Over a ten-year record of aerosol optical properties at SMEAR II

Krista Luoma[1], Aki Virkkula[1,2], Pasi Aalto[1], Tuukka Petäjä[1] and Markku Kulmala[1]

[1]Institute for Atmospheric and Earth System Research, University of Helsinki, Helsinki, 00014, Finland
[2]Finnish Meteorological Institute, Helsinki, 00560, Finland

5 *Correspondence to*: Krista Luoma (krista.q.luoma@helsinki.fi), Aki Virkkula (aki.virkkula@fmi.fi)

Abstract. The aerosol optical properties (AOPs) of particles smaller than 10 µm (PM10) and 1 µm (PM1) have been measured at SMEAR II since 2006 and 2010, respectively. For the PM10 particles the mean values of the scattering and absorption coefficients, single-scattering albedo, and backscatter fraction at λ = 550 nm, and scattering and absorption Ångström exponents at the wavelength ranges 450–700 nm and 370–950 nm were 15.2 Mm^{-1}, 2.1 Mm^{-1}, 0.86, 0.15, 1.80 and 0.94

10 respectively. The time series were used to examine the trends and variation in the AOPs. Statistically significant trends were found for example for the PM10 scattering and absorption coefficients, single-scattering albedo, and backscatter fraction, and the slopes of these trends were -0.342 Mm^{-1}, -0.0952 Mm^{-1}, 3.4·10^{-3}, and 1.3·10^{-3} per year. The tendency for the extensive AOPs to decrease correlated well with the decrease in aerosol number and volume concentration. The tendency for the single-scattering albedo and backscattering fraction to increase affected to the effective aerosol forcing efficiency, indicating that the

15 dry aerosols were scattering the radiation more effectively back into space. In addition to these trends, we also observed seasonal and diurnal variations and variations between the AOPs of the PM1 and PM10 particles.

1 Introduction

Aerosol particles directly affect the climate by scattering and absorbing the shortwave radiation from the sun (ARI, *aerosol–radiation interaction*) (Charlson et al., 1992). The ARI is dependent on the reflectivity of the aerosol particles as well as on

20 the albedo of the surface below the aerosol layer. For the aerosol particles to have a cooling (warming) effect, the reflectivity of the particles must be higher (lower) than the albedo of the surface (Haywood and Shine, 1995). Aerosol particles also impact the climate via aerosol–cloud interactions (ACIs) since aerosol particles may act as cloud condensation nuclei (CCN). By functioning as CCN, aerosol particles also affect the optical properties of the cloud (Haywood and Boucher, 2000). The more CCN are available, the smaller and more numerous are the cloud droplets. Clouds with more droplets scatter light more

25 efficiently, so they have a larger cooling effect than clouds that have fewer droplets (Twomey, 1991). Clouds with smaller droplets have longer lifetimes, since it requires more time for the cloud droplets to grow to the size of rain drops (Lohmann and Feichter, 1997). Longer lifetimes also increase the cooling effect of the clouds.

There are vast uncertainties in determining the global radiative forcing related to aerosol particles (Boucher et al., 2013). The

30 number concentration, chemical composition and size distribution of aerosol particles vary widely both spatially and

temporally, so it is challenging to consider them in the models. Challenges arise even more with the ACIs, which include highly complex processes.

The aerosol optical properties (AOPs) describe how much the particles scatter and absorb radiation at different wavelengths. It is essential to know how the aerosol particles interact with radiation to determine the direct effect on the climate. The extensive optical properties, such as scattering and absorption coefficients, are dependent on the concentration of the particles and also on their size distribution and chemical composition. Intensive properties, however, are not dependent on the concentration but on the properties of the particles, such as the size distribution and composition. Intensive properties can be determined by comparing the scattering, backscattering and absorption measurements at different wavelengths. Therefore, by measuring the AOPs at different wavelengths, we can also obtain information on the size distribution and chemical composition of the aerosol particles and not only on the amount of scattering and absorption. This explains why the measurements of AOPs can give practical results.

In situ measurements of AOPs have been conducted at SMEAR II (Station for Measuring Ecosystem–Atmosphere Relations; Hari and Kulmala, 2005) in Hyytiälä, Finland since 2006 for aerosol particles smaller than 10 µm in diameter (PM10). In addition to the PM10 measurements, AOPs of particles smaller than 1 µm in diameter (PM1) have been measured since 2010. SMEAR II is located in the middle of a pine forest and represents the atmospheric conditions typically found in boreal forests (Hari et al., 2013). Boreal forests are sources for new aerosol particles that are formed in a gas-to-particle conversions (Kulmala et al., 2004; Kulmala et al., 2013). Boreal forests (also known as Taiga) cover approximately 30 % of the world's forests and 8 % of the earth's surface, so they greatly impact the global radiation budget.

Here, we present the observed temporal variation and trends of the AOPs at SMEAR II. These AOPs have been previously discussed by Virkkula et al. (2011) and Pandolfi et al. (2018). Virkkula et al. (2011) used the integrating nephelometer and the aethalometer data from a 3-year period (2006–2009). Pandolfi et al. (2018) compared the aerosol scattering measurements that were conducted at different measurement sites in Europe. At SMEAR II, the study involved nephelometer data, from 2006 to 2015. However, these articles determined the AOPs of the PM10 particles only, and Pandolfi et al. (2018) did not include absorption data. Long time series (2006–2017) of the measurements of both scattering and absorption together at SMEAR II have not been presented before, nor have the optical properties of the PM1 particles.

2 Measurements and methods

2.1 The field site

The measurements presented here were conducted at the SMEAR II station in Hyytiälä, southern Finland (61° 51' N, 24° 17' E, 181 m above sea level.). SMEAR II is located in the middle of a forest that consists mostly of Scots pine (*Pinus sylvestris*

L.) trees (Hari et al., 2013). The nearest larger cities, Tampere (220 000 inhabitants) and Jyväskylä (140 000 inhabitants), are located about 60 km and 100 km from the measurement station. Otherwise, there are no large pollution sources nearby the station.

2.2 Instrumentation

2.2.1 Measurements of aerosol optical properties

AOPs have been measured at SMEAR II since June 2006. The measurements of aerosol scattering, backscattering and absorption coefficients (σ_{sca}, σ_{bsca} and σ_{abs}) were conducted at several wavelengths using an integrating nephelometer (TSI model 3563) and an aethalometer (Magee Scientific model AE-31), since 2013 also with a Multi-Angle Absorption Photometer (MAAP, Thermo Scientific model 5012) and in 2011–2015 with a Particle Soot Absorption Photometer (PSAP, Radiance Research model 3λ-PSAP), and in 2014–2015 extinction was measured with a Cavity-Attenuated Phase Shift apparatus (CAPS, Aerodyne Research model CAPS PMex Monitor). Here, absorption data from the AE-31 and scattering data from the TSI3563 were used since they have the longest time series, and an important part of our discussion is the analysis of trends. Comparison of all optical instruments will be presented in Luoma et al. (manuscript in preparation).

From June 2006 to June 2010, the measurements were conducted for the PM10 particles only and since June 2010 also for the PM1 particles. The sample air is taken through a PM10 inlet (Digitel, Low volume inlet) and led alternatingly either directly to the instruments or via a PM1 impactor.

Until March 2013, the integrating nephelometer and the aethalometer measured sample air that was not dried with any external driers. During winter, the relative humidity (RH) remained below 40 %, since the sample air warmed up to room temperature (about 22 °C). Sometimes in summer, the RH of the sample increased to over the 40 % limit. If the RH was above 40 %, the data were flagged as invalid. After the installation of the Nafion-driers in March 2013, the humidity caused no further problems. A more detailed description of the optical measurements at SMEAR II will be given in Luoma et al. (manuscript in preparation).

2.2.2 Size distribution measurements

In addition to the optical measurements, measurements of the size distribution were used. The size distribution measurements were conducted with a Twin Differential Mobility Particle Sizer (TDMPS) in the size range 3–1000 nm (Aalto et al., 2001) and a TSI Aerodynamic Particle Sizer (APS) in the size range 0.53–10 µm. In the overlapping range of the TDMPS and the APS the number concentrations from the TDMPS were used up to 700 nm. The TDMPS, APS, integrating nephelometer and the aethalometer are located in the same measurement building. The TDMPS and APS have their own individual measurement lines. In the TDMPS measurement line, there is an inlet that removes particles larger than 1 µm. There is no active drying

system in the TDMPS measurement line to prevent particle losses. In the APS measurement line there is a pre-impactor that removes particles larger than 10 µm. The APS has its own drier, which heats up the sample air to above room temperature.

2.3 Data processing

All the data were quality assured manually and averaged for 1 h periods. If the internal RH in the instrument exceeded 40 %,
5 the data from that instrument were excluded from further analysis. All the data were also converted from ambient conditions to the standard temperature and pressure (STP) conditions (1013 hPa, 0 °C). The data used in this study were measured between 21 June 2006 and 31 December 2017, and since that time 81 % of the nephelometer data and 70 % of the aethalometer data were considered valid.

2.3.1 Scattering data

10 The total scattering measured with the nephelometer was corrected for the truncation error according to Anderson and Ogren (1998). We did not apply the truncation correction to the backscattering, since the backscattering measurements were much noisier, especially at the red wavelength.

2.3.2 Absorption data

The aethalometer flow was corrected by comparing the flow reported by the aethalometer with the weekly flow measurements
15 conducted at the station. An average spot size of 8.3 ± 0.1 mm was measured from the old aethalometer filters by using a loupe magnifier (Estenbach) with 0.1 mm accuracy and it was used instead of the spot size reported by the aethalometer.

The absorption measured by the aethalometer was corrected for the filter loading error with the correction algorithms described by Weingartner et al. (2003), Arnott et al. (2005), Virkkula et al. (2007) and Collaud Coen et al. (2010). The measured σ_{sca}
20 values were first interpolated and extrapolated to the AE wavelengths ($\lambda = 370, 470, 520, 590, 660, 880$ and 950 nm). The multiple scattering correction factor ($C_{ref} = 3.34$) was determined, using the MAAP and the AE-31 data. Comparisons and detailed analyses of the algorithms will be presented in Luoma et al. (manuscript in preparation). Here, we used the aethalometer data that were corrected, using the correction algorithm described by Collaud Coen et al. (2010).

25 In calculating the single-scattering albedo, the absorption data had to be interpolated to the same wavelength with the scattering measurements. The absorption data were then interpolated to the green wavelength (550 nm), using the Ångström exponent (α) described in Eqs. 3 and 4.

2.3.3 Intensive optical properties

The extensive properties, which are the scattering, backscattering, and absorption coefficients (σ_{sca}, σ_{bsa}, and σ_{abs}), were used to calculate intensive properties presented in detail below.

5   The single-scattering albedo (ω_0) describes how much of the total light extinction (sum of σ_{sca} and σ_{abs}) caused by the aerosol particles is due to scattering:

$$\omega_0 = \frac{\sigma_{sca}}{\sigma_{sca} + \sigma_{abs}} \tag{1}$$

The ω_0 can be linked with the source and chemical composition of the aerosol particles. High values of ω_0 mean that the aerosol particles are mostly scattering and are light in color. Darker aerosol particles (which have a lower ω_0) have a relatively

10   higher mass fraction of absorbing material, such as soot, which is emitted in combustion processes.

The backscatter fraction (b) describes how much aerosol particles scatter radiation in the backward direction compared with the total scattering

$$b = \frac{\sigma_{bsca}}{\sigma_{sca}}. \tag{2}$$

15   The angular dependency of particle scattering is dependent mostly on the particle size. The value of b is smaller for a size distribution that consists of larger particles, since large particles scatter light heavily in the forward direction and thus b can be used as an indicator of the shape of the particle size distribution. The b is an especially important property for modeling the direct effect of aerosol particles on the climate, since it is used to describe how much sunlight is scattered upwards back into space.

The Ångström exponent (α) is used to describe the wavelength (λ) dependency of a certain optical property (σ) (Ångström, 1929)

$$\alpha = -\frac{\ln\frac{\sigma_1}{\sigma_2}}{\ln\frac{\lambda_1}{\lambda_2}}. \tag{3}$$

After calculating α, the optical property can be extrapolated or interpolated into different wavelengths

25   $$\sigma_1 = \sigma_2 \left(\frac{\lambda_1}{\lambda_2}\right)^{\alpha}. \tag{4}$$

In this study, α values were calculated for σ_{sca} and σ_{abs} to obtain α_{sca} and α_{abs}.

Since light scattering is highly dependent on particle size, α_{sca} is also used as an indicator of the particle size distribution and is larger for the smaller particles, since they have a stronger wavelength dependency. If α_{sca} is larger than 2, it is typically

30   believed that the volume distribution is dominated by particles smaller than 0.5 µm, and if α_{sca} is smaller than 1, the larger

particles (physical diameter $D_p > 0.5$ µm) predominate in the distribution (Schuster et al., 2006). In comparison to b, α_{sca} is more sensitive to the coarse mode particles (e.g. Collaud Coen et al., 2007).

The value of α_{abs} is also dependent on the chemical composition, coating, and size of the particles, even though the chemical composition is generally considered to be the more important factor. The α_{abs} is usually used to identify black carbon (BC) and brown carbon (BrC) particles. The BC particles are highly absorbing aerosol particles and the BrC particles are considered to consist of some organic carbon compounds, which absorb light more strongly at short than long wavelengths. If the particles consist purely of BC, the absorption would be dependent on wavelength as λ^{-1} and α_{abs} would be equal to unity. However, if the particles also consist of material that absorbs light only at ultraviolet wavelengths, α_{abs} would be larger than 1. In ageing processes the BC particles may become coated by some purely scattering material, such as sulfuric acid or ammonium sulfate, or by slightly absorbing organic material (Schnaiter et al., 2005; Zhang et al., 2008). The coating greatly affects the absorption wavelength dependency, and thus the division into BC and BrC by considering only α_{abs} is not that simple. If the sizes of the BC particles and the thickness and complex refractive index (m) of the coating are not known, it is challenging to use α_{abs} to describe the chemical composition of the particles (Gyawali et al., 2009; Lack and Cappa, 2010). The absorption wavelength dependency is also used to describe the source of the BC (Sandradewi et al., 2008; Zotter et al., 2017). The source apportionment assumes that there are BC emissions only from traffic and wood burning and that the BC from these sources has a specific wavelength dependency.

To investigate how the AOPs at SMEAR II would affect the climate, the aerosol radiative forcing efficiency ($\Delta F \delta^{-1}$ or RFE) was also calculated. The RFE describes how large a difference the aerosol particles would make to the radiative forcing (ΔF) per unit of aerosol optical depth (δ)

$$\frac{\Delta F}{\delta} = -D\, S_o\, T^2\, \omega\, \beta\, (1 - A_c) \left[(1 - R_s)^2 - \left(\frac{2R_s}{\beta}\right)\left(\frac{1}{\omega_0} - 1\right) \right]. \tag{5}$$

In the equation, D is the fractional day length, S_0 the solar constant, T the atmospheric transmission, A_C the fractional cloud amount, and R_S the surface reflectance for which the following constants were used respectively: $D = 0.5$, $S_0 = 1370$ Wm^{-2}, $T = 0.76$, $A_C = 0.6$ and $R_S = 0.15$. The values were chosen according to the article by Haywood and Shine (1995). The factor β is the upscatter fraction and is calculated using b (Delene and Ogren, 2002)

$$\beta = 0.0817 + 1.8495b - 2.9682b^2. \tag{6}$$

It must be noted that ω_0 and b used in Eq. 5 are defined for dried sample air; thus RFE does not represent ambient air. In the ambient air, RH is larger and the particles may have different optical properties due to hygroscopic growth.

2.4 Properties calculated from particle size distributions

With the size distributions it is possible to calculate differently weighted mean diameters. In this study, we used the geometric mean diameter (GMD) and the volume mean diameter (VMD). The GMD is the mean diameter that is weighted by the number concentration

$$GMD = \exp\left(\frac{\sum N_i \ln D_{p,i}}{\sum N_i}\right),\tag{7}$$

while the VMD is weighted by the particle volume

$$VMD = \frac{\sum D_{p,i} V_i}{V_{tot}} = \frac{\sum N_i D_{p,i}^4}{\sum N_i D_{p,i}^3}.\tag{8}$$

Since the number concentration is focused on the nucleation and Aitken mode particles, the GMD describes the distribution changes in the smallest sizes. The VMD, in contrast, is affected by the changes in the accumulation and coarse mode, since they contribute the most to the volume size distribution.

The measurements of the AOPs and size distribution can be combined by determining the complex refractive index ($m = n + ik$), which describes how much the particles scatter and absorb light and can be used to model σ_{sca}, σ_{bsca} and σ_{abs} from the size distribution measurements. Index m consists of the real part (n), which accounts for the scattering, while the absorption is described by the imaginary part (k). Like ω_0, m describes the darkness and the chemical composition of the aerosol particles.

In this study, m was iterated from the σ_{sca}, σ_{abs} and size distribution measurements in a manner similar to that described by Virkkula et al. (2011). In the first step of the interpolation $\sigma_{sca,Mie}$ and $\sigma_{abs,Mie}$ were determined for the measured size distribution by using the Mie-theory with initial $m = 1.544 + 0.019i$. The calculated $\sigma_{sca,Mie}$ and $\sigma_{abs,Mie}$ were then compared with the measured σ_{sca} and σ_{abs}. If the calculated and measured values did not agree the real part of m was first varied stepwise by 0.001 until the measured and modeled σ_{sca} agreed. Next, the imaginary part of m was varied in the same way until the measured and modeled σ_{abs} agreed. The new imaginary part of m also affected σ_{sca} so the real part had to be reiterated. This iteration was continued until the measured and calculated values agreed within 1 %. The MATLAB codes developed by (Mätzler, 2002) were used to model the Mie scattering and absorption.

2.5 Trends

The trends and their significance were determined using the seasonal Kendall test described by Gilbert (1987). This test determines if there is a similar trend for each season (month) separately. All of the trends were calculated for the monthly medians, and at least 14 days of valid data in a given month were required for this month to be taken into account in the trend analysis.

3 Results and discussion

Below we first present the descriptive statistics of the AOPs, their trends, and seasonal variations at SMEAR II for both the PM1 and PM10 measurements. The figures of the AOPs in this chapter are presented in the green wavelength (550 nm for the scattering and intensive properties and 520 nm for the absorption measurements). In the figures of α_{sca} and α_{abs}, wavelength ranges of 450–700 nm and 370–950 nm were used.

3.1 Overview of the data

The descriptive statistics of the AOPs of both the PM10 and PM1 particles are shown in Tables 1 and 2, respectively. From Table 1 we see that the PM10 AOPs differ somewhat from the results of Virkkula et al. (2011) and Pandolfi et al. (2018), which can be explained by the trends and by differences in the data processing. For example the mean σ_{sca} (~15 Mm^{-1}) at λ = 550 nm in this study was lower than that presented by Virkkula et al. (2011) (~18 Mm^{-1}) and by Pandolfi et al. (2018) (~17 Mm^{-1}), which is probably due to the tendency of σ_{sca} to decrease (see Sect. 4.2). However, we also determined a strong tendency for σ_{abs} to decrease as well, but the mean σ_{abs} (~2.1 Mm^{-1}, interpolated to 550 nm) was not much lower than the mean (~2.2 Mm^{-1}, at 550 nm) in the study by Virkkula et al. (2011). This was mainly due to the different aethalometer data-processing algorithms and different C_{ref} values used. Virkkula et al. (2011) used the algorithm of Arnott et al. (2005) and C_{ref} = 3.688 at λ = 520 nm. C_{ref} was wavelength-dependent as in Arnott et al. (2005). Naturally, the different methods used in the absorption data processing also affected the optical properties, which are dependent on the σ_{abs}, such as ω_0 and k.

In comparison to similar studies conducted at other Finnish measurement stations at Pallas in northern Finland (Lihavainen et al., 2015) and at Puijo tower in Kuopio, eastern Finland (Leskinen et al., 2012), SMEAR II showed the highest σ_{sca} and σ_{abs} measured for PM10 particles. At SMEAR II, σ_{sca} was about two times higher and σ_{abs} more than five times higher than at Pallas. The Pallas station is remote, located 170 km north of the Arctic Circle, far from anthropogenic sources. At SMEAR II, σ_{sca} and σ_{abs} were about 1.4 and 1.1 times higher, respectively, than that measured at the Puijo tower, even though the Puijo tower is a semi-urban measurement station located only 2 km away from the Kuopio city center. At the Puijo tower the measurements were conducted only on particles smaller than 2.5 µm, which explains part of the differences, at least for σ_{sca}. The median ω_0 was 0.85 for Puijo and 0.87 for SMEAR II and for the remote Pallas station notably higher (0.93).

The differences between the optical properties of the PM1 and PM10 particles are explained by the differences in concentrations, size distributions and chemical compositions. The average values of the PM10 particles given in Table 1 are from the entire measurement period. If only the PM10 data overlapping with the PM1 measurements were taken into account, the median values of σ_{sca}, σ_{abs}, ω_0, b, α_{sca}, α_{abs}, n, and k would have been 9.5 Mm^{-1}, 1.3 Mm^{-1}, 0.88, 0.15, 1.92, 0.96, 1.523 and 0.014 ($\sigma_{sca,}$, ω_0, b, α_{sca}, n and k at 550 nm, σ_{abs} at 520 nm), respectively. The extensive variables (σ_{sca}, σ_{bsca} and σ_{abs}) were smaller for the PM1 measurements, since there was less particle volume interacting with the radiation. Due to the differences in the

median ω_0 and n, the PM1 particles absorbed more light relative to scattering than the PM10 particles. The α_{sca} and b are related to the sizes of the particles, so they were naturally different between the PM1 and PM10 particles. For the smaller PM1 particles, the α_{sca} and b were larger than for the PM10 particles. However, b does not have as large a difference between the PM1 and PM10 particles as α_{sca}.

5   3.2 Trends

The monthly medians of the AOPs at SMEAR II are shown in Fig. 1. The monthly medians are marked in Fig. 1 only if the month had at least 14 days of valid data. The time series were used to determine the trends for the optical properties. The slopes of the trends and the trend statistics are presented in Table 3. The table also presents the trends as percentages that were calculated by dividing the slope by the overall median value of the variable. The trends are also plotted in Fig. 1 The trends

10   were determined for both the PM10 and PM1 measurements.

In the extensive properties, the trends were negative for the PM10 and PM1 measurements. The slopes of the trends for PM10 σ_{sca}, σ_{bsca} and σ_{abs} were -0.34, -0.043, and -0.095 Mm^{-1}yr^{-1}, respectively. These decreases in the extensive properties were due to decrease in the particle number concentration, which can be seen in the TDMPS and APS data shown in Fig. 2. Pandolfi et

15   al. (2018) also showed a statistically significant trend for σ_{sca} (-0.588 Mm^{-1}yr^{-1}) that was slightly more negative than our results. They also reported negative trends at other European sites. The results are in line with the decrease in particle number concentration observed in European countries (Asmi et al., 2013).

The trends of the intensive optical properties were also investigated. These trends describe how properties such as the size

20   distribution and chemical composition of the aerosol particles have changed. For the PM1 b and α_{sca} the trends were positive, indicating that the weight in the size distribution was moving towards smaller particles. For the α_{sca} only the PM1 particles showed a statistically significant positive trend; however, the p-value for PM10 α_{sca} trend was below 0.10, so there was weak evidence for the positive trend in PM10 α_{sca} as well. Since the trends for the PM10 and PM1 measurements were similar, the trends in α_{sca} and b may indicate that the concentration of larger particles in the accumulation mode was decreasing. The

25   changes in the size distribution were investigated by determining a trend for each TDMPS and APS measurement channels. The results are shown in Fig. 3, which supports the claim that especially the largest accumulation mode particles were experiencing the relatively greatest decrease. In Fig. 2 it can be seen that VMD and particulate volume (V, calculated for particles smaller than 1 µm) also showed statistically significant negative trends, which also support the tendency of b and α_{sca} to increase.

For ω_0, the trend was positive, showing that the aerosol particles were absorbing relatively less light than before. As shown by the positive trend in ω_0 and the negative trend in extensive properties, the air measured at SMEAR II was cleaner than before, while the higher ω_0 indicates that the measurements were less affected by particles produced by incomplete combustion. The

negative trend for k supports the tendency for ω_0 to increase, since the negative trend for the imaginary part of m means that particles absorb less light. The α_{abs}, which is also related to the chemical composition of the particles, showed no significant trend for either the PM1 or PM10 particles. The negative trend for the interpolated n was only significant for the PM1 particles. The tendency for the interpolated n to decrease could have been caused by changes in the chemical composition.

For the PM10 measurements, the Nafion-driers were installed in 2010, which decreased the RH in the measurement line. The change in RH may have resulted in some changes in particle sizes, especially if the particles were hygroscopic. A Nafion-drier can also increase the deposition of the particles, which then lowers the number concentration. Thus, installation of the Nafion-driers may have resulted in lower values in the extensive properties. However, the trends were similar for the PM10 and PM1

10 particles. During the PM1 measurements, there were no large changes in the measurement line, so the observed trends were probably not caused by any technical changes in the measurement line.

As can be seen in the Fig. 1, all the properties have some gaps in the data. Most of these gaps in the time series of σ_{sca}, σ_{bsca} and σ_{abs} during the summers of 2009 and 2010 were due to too high RH. The gap in 2010 was due to maintenance and

15 installation of the driers and the switching inlet system. Some additional σ_{bsca} data were missing, due to malfunction of the backscatter shutter of the integrating nephelometer. Dirty optics, malfunctions and maintenance caused the gaps in the aethalometer data in 2012 and 2015.

3.3 Aerosol optical properties and size distribution

To obtain a better view on how the shape of the size distribution affects the AOPs, the various AOPs were compared against

20 the GMD and VMD separately for the PM1 and PM10 measurements. The results of the comparison are shown in Fig. 4. The GMD was mostly affected by the small nucleation and Aitken mode particles, which are high in number concentration, but was also affected by accumulation mode particles. The VMD, however, was heavily affected by the size distribution of the accumulation and coarse mode particles, since they predominated in the particle volume size distribution. This explains why there was no large difference between the GMD for the PM1 and PM10 particles, while for the VMD the difference is much

25 higher.

For both the PM10 and PM1 particles, there was a clearly positive correlation between the σ_{sca} and GMD, which was due to the changes in particle concentration in the accumulation mode. The median number and volume size distribution for situations when GMD was below 50 nm or above 100 nm are presented in Figs. 5c and d. There was a clear difference in the number

30 and volume size distribution in the accumulation mode when the GMD limit is varied. From the number size distribution, it can be seen that GMD increased due to a larger accumulation mode and lack of particles in the nucleation and Aitken modes. Nucleation and Aitken mode particles are produced and grown by condensing vapors and since larger particles in the accumulation mode act as a condensation sink for vapors, the smaller particle modes do not tend to exist when accumulation

mode particles are present. By comparing Figs. 5c and d, it can be seen that the coarse mode particles did not significantly affect the GMD. The positive correlation between σ_{sca} and GMD is in line with the small positive correlation between the ω_0 and GMD as well, since the scattering increases with higher GMD.

5   For the PM10 particles, there was a negative correlation between the σ_{sca} and VMD, but when the coarse particles were ignored, the correlation became positive. The negative correlation for the PM10 particles is caused by the changes in the accumulation and coarse mode particle concentration. This is shown in further detail in Fig. 5a, where the median volume size distribution is presented for situations in which the VMD > 1500 nm, 500 nm < VMD < 1000 nm and VMD < 500 nm. When the VMD was high there was a strong coarse mode but the accumulation mode was clearly smaller than in the other situations. Even

10   though the VMD was high, the lack of accumulation mode particles decreased the scattering. From Fig. 4, it can be seen that the σ_{sca} became maximal when the VMD was about 500–1000 nm. In this VMD range, the coarse mode was slightly smaller but the accumulation mode clearly increased, thus increasing the scattering. When the VMD < 500 nm, the coarse mode was almost completely missing, which decreased the σ_{sca} even though there was a large accumulation mode present.

15   The size-dependent properties α_{sca} and b acted rather differently when compared with the GMD and VMD. When the GMD was higher, the α_{sca} also increased, which contrasted with the expectation that the α_{sca} would decrease when the size distribution is dominated by larger particles. The observation that the α_{sca} increased with an increasing GMD is in line with the analyses made for AOPs and size distributions measured in Guangzhou, China by Garland et al. (2008), at SMEAR II by Virkkula et al. (2011), and in Nanjing, China by Shen et al. (2018). For unimodal size distributions the α_{sca} decreased with increasing

20   GMD, as is shown by the lines in Fig. 4. They were calculated by generating unimodal size distributions with the geometric standard deviations GSDs = 1.5 and 2.0 and calculating the σ_{sca} for λ = 450, 550, and 700 nm with the Mie code with m = 1.517 + 0.19i and the α_{sca} from them. For bimodal size distributions, the relationship may be the opposite as Schuster et al. (2006) showed. At SMEAR II the size distribution typically consisted of multiple modes (Dal Maso et al., 2005; Saarikoski et al., 2005) which explains the observed relationship. An additional qualitative analysis of this relationship is given in Fig. 5c,

25   where the median number and volume size distributions are plotted for situations in which the GMD was < 50 nm and > 100 nm. By comparing these two situations, it can be seen that when the GMD > 100 nm the accumulation mode was much larger than when GMD < 50 nm. Since the coarse mode is rather similar for both cases, the α_{sca} varied due to changes in the accumulation mode. For the α_{sca} and VMD, the correlation was negative (Fig. 5), which supports the expectations. However, the α_{sca} measured for the PM10 particles was much higher than that modeled for the unimodal distributions, which can also be

30   explained by the multiple modes of the real size distributions. For the PM1 particles, the α_{sca} measurements were well in line with the values modeled, since the coarse mode particles were removed prior to the measurements and the VMD described better how the accumulation mode shifted.

There was a negative correlation between the GMD and b, which was expected, especially since the size distribution was unimodal, as shown with the lines calculated for the above-explained simulated unimodal size distributions. However, the correlation between the GMD and b was rather weak, most probably due to the multimodality of the size distributions, as also for α_{sca}. The correlation between the b and VMD was different for the PM1 and PM10 particles. The correlation for the PM1

5   particles was clearly negative as expected, but for the PM10 particles the correlation was positive. The explanation for the positive correlation is linked with the multimodality of the size distributions. This effect was not observed with the PM1 particles, because there were no coarse particles dominating VMD. The different correlations of α_{sca} and b with VMD for the PM10 particles indicates that the α_{sca} and b were sensitive to different size ranges. This is in line with Collaud Coen et al. (2007), who stated that in the Jungfraujoch data, b was sensitive to particles smaller than 400 nm and that the sensitivity of the

10   α_{sca} was at its maxima for particle diameters between 500 and 800 nm.

3.3.1 Variation in refractive index during new particle formation

When the AOPs were plotted in a time series with the size distribution (Fig. 6), we observed that the iterated real part of the m drops often decreased during new particle formation (NPF) event days. During a NPF event day, new particles are formed in the nucleation mode. After formation the particles grow, which is shown by the high concentration stripes in the size

15   distribution time series. The interesting observation is that typically n decreased greatly, often down to < 1.4 few hours after the NPF event starts. In Fig. 6, the decrease can be seen on every event day, but not on 31 April 2013, when the concentration was higher. After the decrease, n grew at the same time as the newly-formed particles grew. After the growth finished $n \approx 1.52$ which is approximately the refractive index of ammonium sulfate.

20   The reason for this behavior is unknown, since the new particles were much smaller than the smallest optically active particles (100 nm). The data suggest that the condensable vapor that makes the newly-formed particles grow had a low n, because when this vapor condensed also on the accumulation mode particles, iterated n also decreased. During growth, n increased suggesting the condensable vapor differs at the various different stages of the growth. It has been shown that low-volatility organics play an important role in the growth of particles in forests (e.g., Ehn et al., 2014), so they may be the explanation. It is also worth

25   noting that a similar phenomenon was observed in Antarctic NPF by Virkkula et al. (2006). For the other AOPs, we observed no clear differences for event and non-event days.

3.4 Seasonal variation

The seasonal variation in the AOPs was clearly visible in the 12-year record shown in Fig. 7. The seasonal variation in σ_{sca} and σ_{bsca} was not yet as clear in Virkkula et al. (2011) as it is now. For the σ_{sca} and σ_{bsca}, there were two local maxima that occurred

30   during late winter (February) and late summer (July). The local minima occur during spring (April) and late autumn (October). The σ_{abs} showed the highest values during winter (February) and the lowest values during summer (June).

For the extensive properties, the highest values occurred at the same time in winter (February) when the ω_0 was also low, which means that there were larger amount of particles from anthropogenic sources than in summer. Long-range transport brings pollution from the central and eastern Europe (Hyvärinen et al., 2011; Virkkula et al., 2011) especially in winter when

5   the polar front has moved southward. Hienola et al. (2013) estimated that about 30 % of the measured equivalent black carbon (eBC, the BC concentration determined optically from σ_{abs} measurements) at SMEAR II is transported from outside the borders of Finland. It means that in Hyytiälä, about 70 % of the absorbing aerosol mass is emitted from local or regional sources or transported from Finnish cities. Since February is one of the coldest months in Finland, domestic wood burning in the local and regional area increases the particle concentration (Karvosenoja et al., 2011). Pollution can also be transported from nearby

10 cities (the largest and closest are Tampere and Jyväskylä). Hyvärinen et al. (2011) observed no remarkable changes in the Hyytiälä eBC concentrations coming from the Tampere region. However, the largest concentrations they observed came from the direction of Orivesi, which is a smaller town (population about 9 000) 20 km from the measurement station.

In summer, the ω_0 had its highest values since the σ_{sca} was high and the σ_{abs} was low. In summer, the anthropogenic influence

15 is not as strong as in the winter since the energy consumption is lower. The contribution of particles from natural sources increased during spring and summer when the vegetation was active and growing. The seasonal variation in the n and k was clearly associated with the ω_0. In summer when the ω_0 was high, n was high and k was low. In winter, the relationship was the opposite. The scattering maximum in summer was probably caused by secondary organic particles (Tunved et al., 2006), which explains why the b and α_{sca} are also maximal.

There is an anti-correlation between the seasonal variations of ω_0 and α_{abs}. The maximum values of α_{abs} (> 1) occur in winter, which means that light is absorbed more efficiently at shorter wavelengths than in summer. A higher α_{abs} may suggest that light is absorbed not only by BC, but also by some light-absorbing organic carbon compounds, i.e. brown carbon (BrC). In summer, α_{abs} was often < 1 but the deviation was large. Values below 1 could be caused by large BC particles (D_p > 100 nm)

25 that have a purely scattering coating (Lack and Cappa, 2010). In using only α_{abs}, it is difficult to determine if the particles consist of BrC, since BC particles with coating can also have an α_{abs} up to 1.6 (Lack and Cappa, 2010). In Fig. 7 we can see that the value of 1.6 is not really reached in Hyytiälä. Since α_{abs} is dependent on the size of the BC core, the thickness of the coating and the m of the coating, more detailed investigation would be needed to determine why α_{abs} is varies.

30 The seasonal variation in α_{sca} and b describes the seasonal variation in the size distribution of the particles. Both α_{sca} and b were maximal in summer and minimal in winter, suggesting that the particle population consisted of fewer large particles in winter than in summer. For example, this could have been caused changes in the largest accumulation mode particles as it did in the trend analysis.

3.5 Diurnal variation

There was also some diurnal variation in AOPs at SMEAR II, as shown in Fig. 8. However, the diurnal variation was rather weak and not nearly as clear as the seasonal variation. Since the meteorological conditions at the SMEAR II station vary widely from season to season, the daily variation was determined separately for spring (March–May), summer (June–August), autumn (September–November) and winter (December–February). The diurnal variation is shown in further detail in the supplementary material.

For the extensive properties, the daily variation was similar in spring and summer, when both the σ_{sca} and σ_{abs} experienced a decrease during the day. The plausible explanation is boundary layer mixing, which dilutes the air. The diurnal variation in both the σ_{sca} and σ_{abs} was smallest in autumn. In winter, the σ_{sca} was maximal before noon but it did not decrease significantly in the afternoon, which is clearly different from the diurnal cycles of the σ_{sca} in spring and summer. In winter, the variation was much weaker which can be explained by the weaker solar radiation and consequently weaker boundary layer mixing. In winter, there were also more often temperature inversions that caused air pollutants to accumulate in the boundary layer. The maximum σ_{abs} in winter was observed in the evening at about 18–20 local time, whereas the maximum σ_{sca} was before noon. In winter, the extensive properties increase slightly during the day and decrease during the late night and early morning hours. The daily variation in the ω_0 is contrasted with the variation in σ_{abs} in every season. In spring, summer, and autumn ω_0 was the highest during the day, while in winter $_{it}$ peaked in the early morning.

3.6 Variation between the PM10 and PM1 measurements

Even though the average values between the optical properties of the PM10 and PM1 particles differed, their seasonal variation was similar for all the various properties as can be seen in Fig. 7. However, there was a seasonal variation in the relationship between the PM10 and PM1 extensive properties, as shown in Fig. 9. The seasonal variation in the PM1/PM10 ratio describes the impact of the coarse and fine particles on the σ_{sca} and σ_{abs}.

For the σ_{sca} the seasonal variation in the PM1/PM10 ratio was clear, but for the σ_{abs} there seemed to be no seasonal variation in the ratio whatsoever. The seasonal medians of the PM1/PM10 σ_{sca} varied from 0.7 to 0.8, and on average submicron particles caused about 75 % of the total scattering of the PM10 particles. This was apparently a lower fraction than in the previous analysis of SMEAR II scattering data. Virkkula et al. (2011) stated that the seasonal average contributions of submicron particles to the total σ_{sca} was in the range of 88–92 % , clearly more than in the present work. However, in that study the scattering size distribution and the contributions of the various size ranges were calculated from particle number size distributions with a Mie model and the physical diameters (D_p) were used whereas here the PM1 corresponds to particles smaller than the aerodynamic diameter D_a of 1 µm. With particle density of 1.7 g cm^{-3} this corresponds to the physical diameter $D_p = (1/1.7)^{\frac{1}{2}}$ 1 µm $\approx$ 0.77 µm. The contribution of particles smaller than 0.77 µm is approximately 85 % if it is estimated from

Fig. 11 of Virkkula et al. (2011), still more than the ~75 % contribution of submicron scattering shown here. This may have resulted from the cutoff diameter of the PM1 impactor is not exactly sharp and also that the particles entering the impactor may have still been somewhat moist and thus larger than their dry size and were therefore removed from the sample stream. Further analysis of the difference is omitted here.

The maxima of the submicron particle scattering occurred in winter and summer. The summer peak coincided with the maxima of the PM10 α_{sca}, which already indicates that smaller particles play a major role in the size distribution. However, this correlation between the PM1/PM10 ratio and α_{sca} was not observed in winter. In Fig. 2, it can be seen that the VMD for the PM1 particles peaked during the winter, which is an indicator of a relatively larger accumulation mode. The large accumulation

10 mode caused α_{sca} to be low, even though there was relatively less scattering by the coarse particles.

For the σ_{abs}, the median of the PM1/PM10 ratio did not greatly vary seasonally. The PM1 particles absorbed about 90 % of the total PM10 particle absorption. So for the σ_{abs} there were no large difference in the σ_{abs} of the PM1 and PM10 particles. The coarse mode particles are typically primary and they have a quite high ω_0 so their absorption is minor compared with the PM1

15 particles. The soot particles, which account for most of the particulate absorption, are typically submicron particles. The deviation, however, clearly varied seasonally. In summer, the variation was considerably higher than in winter. This was probably due to the low σ_{abs} and high σ_{sca} in summer. Large amounts of particles with high ω_0, cause uncertainties in the measurements. Especially when the σ_{abs} is low in summer, the errors were relatively higher. The uncertainty in the measurements also explains why there were so many values above 1 measured in the PM1/PM10 σ_{abs} ratio. The evolution of

20 the PM1/PM10 ratio was also investigated but the trends determined for both the σ_{sca} and σ_{abs} were not significant.

3.7 Radiative forcing efficiency

For the aerosol radiative forcing efficiency (RFE = $\Delta F \delta^{-1}$) the trends and seasonal variation were also investigated, as shown in Fig. 10. Both the ω_0 and b tended to increase, which makes the RFE decrease. The decreasing RFE means that the properties of dry aerosol particles have changed so that they cool the climate more efficiently.

The seasonal variation ine the RFE also followed the seasonal cycles of the ω_0 and b. The RFE was minimal in summer and maximal in winter. Since b was lowest (forward-scattering particles) and the ω_0 is also low (dark particles) in winter, the particles clearly did not have as strong a cooling effect as in summer when particles are smaller and light colored. The RFE did not take into account the variations in D, T_{at}, A_C or R_S, which clearly vary seasonally. The D, for example is much smaller

30 during the winter, which would have lowered the RFE; in contrast, however, the R_S is much higher when there is snow cover and would make the RFE increase.

The relationship between the RFE, ω_0 and b is shown in Fig. 11. It can be seen that the correlation with ω_0 is much stronger than with b. This can be interpreted such that at SMEAR II, the RFE was much more dependent on the chemical composition described by the ω_0 and not as much on the size distribution described by b.

5   The RH of the ambient air was also not taken into account, and the RFE was calculated for dry aerosol particles. If the particles were embedded in moist ambient air, they would have experience hygroscopic growth (Birmili et al., 2009) and thus their σ_{sca} would have been enhanced. In ambient air, we should take into account the variability in RH, most importantly as a function of height. At the top of the boundary layer we typically have RH values close to 100 %. Zieger et al. (2015) measured a 1.6 times larger σ_{sca} for moist air (RH = 0.85 %) at SMEAR II. With the available instruments it was not possible to measure how

10 the σ_{abs} changes with increasing RH. Due to the enhanced scattering (higher ω_0) the RFE would be more negative for the aerosol particles embedded in air with higher RH. Even though the simplified RFE does not give an absolute value for the aerosol forcing, it can still be used as an indicator of how the properties of the aerosol particles have been changing and what type of a direct effect the changes have on climate.

15 The RFE describes only the efficiency of the aerosol particles in cooling or warming the climate. Even if the RFE was very negative, the influence of aerosol particles on the climate would be small if the optical depth (δ) was small. The δ is highly dependent on the σ_{sca} and σ_{abs}. This is analyzed in further detail in Fig. 12, where the ω_0 is presented as a function of b. In Fig. 12 the RFE is presented with isolines and the σ_{sca} is presented by color coding. Figure 12 shows that when the RFE is most negative, the median σ_{sca} is actually experiencing its lowest value. When the RFE is closest to zero, the median σ_{sca} is the

20 highest. It is also seen that when the b is high and the particle size distribution consists of smaller particles, ω_0 is smallest and the particles are most efficient at cooling the atmosphere. These relationships were also observed in a study of AOPs at the Station for Observing Regional Processes of the Earth System (SORPES), a measurement station in Nanjing China (Shen et al., 2018).

4 Conclusions

25 In this study, we presented over 11-year long time series of AOPs measured at SMEAR II, a station in southern Finland. With the long time series, it was possible to see statistically significant trends, seasonal and diurnal variations and different types of causality between the optical properties. We also compared the AOPs with the aerosol size distribution measurements conducted at the station. In comparing the AOPs and size distribution, we were able to determine the m values and observe in greater detail how the AOPs are dependent on the shape of the size distribution.

The extensive AOPs, as well as the aerosol number and volume concentration, tended to decrease This tendency for the extensive properties to decrease and for the ω_0 to increase suggests that the amount of aerosol particles from anthropogenic

sources has been decreasing since 2006. This could be an outcome of emission standards and implementation of new, cleaner technologies. The tendency for b and α_{sca} to increase indicate that the particle size distribution is gaining more weight with the smaller diameters, due to a decreasing number of particles on the larger side of the accumulation mode. Since the aerosol particles are smaller and less dark than before, their RFE is more negative, which means that the ability per unit δ to cool the

5   atmosphere has increased. However, since the extensive properties and particle number concentration are decreasing the total aerosol forcing is probably also decreasing.

There are clearly seasonal variations in the AOPs. The largest differences occur during summer and winter. The seasonal variations in the extensive properties and ω_0 revealed that in winter the particles have a larger contribution from the

10   anthropogenic sources than during summer. The aerosol RFE was calculated, using constant values in the fraction of the day, surface albedo, atmospheric transmission and cloud fraction, which clearly show seasonal variations in southern Finland. The variations in the sun elevation angle were also not taken into account. Determining a more realistic RFE would require more work on the topic.

15   The diurnal variations at the SMEAR II station are most probably due to boundary layer development and the diurnal variations during spring and summer could not be explained by anthropogenic activities. During winter, however, the boundary layer development is not as strong and the anthropogenic influence can then also be seen even at the remote SMEAR II station.

References

Aalto, P., Hämeri, K., Becker, E., Weber, R., Salm, J., Mäkelä, J. M., Hoell, C., O'dowd, C. D., Hansson, H.-C., and Väkevä, M.: Physical characterization of aerosol particles during nucleation events, Tellus B: Chemical and Physical Meteorology, 53, 344-358, 2001.

5 Anderson, T. L., and Ogren, J. A.: Determining aerosol radiative properties using the TSI 3563 integrating nephelometer, Aerosol Science and Technology, 29, 57-69, 1998.

Arnott, W. P., Hamasha, K., Moosmüller, H., Sheridan, P. J., and Ogren, J. A.: Towards aerosol light-absorption measurements with a 7-wavelength aethalometer: Evaluation with a photoacoustic instrument and 3-wavelength nephelometer, Aerosol Science and Technology, 39, 17-29, 2005.

10 Asmi, A., Collaud Coen, M., Ogren, J., Andrews, E., Sheridan, P., Jefferson, A., Weingartner, E., Baltensperger, U., Bukowiecki, N., and Lihavainen, H.: Aerosol decadal trends–Part 2: In-situ aerosol particle number concentrations at GAW and ACTRIS stations, Atmospheric Chemistry and Physics, 13, 895-916, 2013.

Birmili, W., Schwirn, K., Nowak, A., Petäjä, T., Joutsensaari, J., Rose, D., Wiedensohler, A., Hämeri, K., Aalto, P., and Kulmala, M.: Measurements of humidified particle number size distributions in a Finnish boreal forest: derivation of 15 hygroscopic particle growth factors, Boreal Environment Research, 14, 458-480, 2009.

Boucher, O., Randall, D., Artaxo, P., Bretherton, C., Feingold, G., Forster, P., Kerminen, V.-M., Kondo, Y., Liao, H., and Lohmann, U.: Clouds and aerosols, in: Climate change 2013: the physical science basis. Contribution of Working Group I to the Fifth Assessment Report of the Intergovernmental Panel on Climate Change, Cambridge University Press, 571-657, 2013.

Charlson, R. J., Schwartz, S., Hales, J., Cess, R. D., Coakley, J. J., Hansen, J., and Hofmann, D.: Climate forcing by 20 anthropogenic aerosols, Science, 255, 423-430, 1992.

Collaud Coen, M., Weingartner, E., Nyeki, S., Cozic, J., Henning, S., Verheggen, B., Gehrig, R., and Baltensperger, U.: Long-term trend analysis of aerosol variables at the high-alpine site Jungfraujoch, Journal of Geophysical Research: Atmospheres, 112, 2007.

Collaud Coen, M., Weingartner, E., Apituley, A., Ceburnis, D., Fierz-Schmidhauser, R., Flentje, H., Henzing, J., Jennings, S. 25 G., Moerman, M., and Petzold, A.: Minimizing light absorption measurement artifacts of the Aethalometer: evaluation of five correction algorithms, Atmospheric Measurement Techniques, 3, 457-474, 2010.

Dal Maso, M., Kulmala, M., Riipinen, I., Wagner, R., Hussein, T., Aalto, P. P., and Lehtinen, K. E.: Formation and growth of fresh atmospheric aerosols: eight years of aerosol size distribution data from SMEAR II, Hyytiala, Finland, Boreal Environment Research, 10, 323-336, 2005.

30 Delene, D. J., and Ogren, J. A.: Variability of aerosol optical properties at four North American surface monitoring sites, Journal of the Atmospheric Sciences, 59, 1135-1150, 2002.

Ehn, M., Thornton, J. A., Kleist, E., Sipilä, M., Junninen, H., Pullinen, I., Springer, M., Rubach, F., Tillmann, R., and Lee, B.: A large source of low-volatility secondary organic aerosol, Nature, 506, 476, 2014.

Garland, R., Yang, H., Schmid, O., Rose, D., Nowak, A., Achtert, P., Wiedensohler, A., Takegawa, N., Kita, K., and Miyazaki, 35 Y.: Aerosol optical properties in a rural environment near the mega-city Guangzhou, China: implications for regional air pollution, radiative forcing and remote sensing, Atmospheric Chemistry and Physics, 8, 5161-5186, 2008.

Gilbert, R. O.: Statistical methods for environmental pollution monitoring, John Wiley & Sons, 1987.

Gyawali, M., Arnott, W., Lewis, K., and Moosmüller, H.: In situ aerosol optics in Reno, NV, USA during and after the summer 2008 California wildfires and the influence of absorbing and non-absorbing organic coatings on spectral light absorption, Atmospheric Chemistry and Physics, 9, 8007-8015, 2009.

5   Hari, P., and Kulmala, M.: Station for Measuring Ecosystem–Atmosphere Relations, Boreal Environment Research, 10, 315-322, 2005.

Hari, P., Nikinmaa, E., Pohja, T., Siivola, E., Bäck, J., Vesala, T., and Kulmala, M.: Station for measuring ecosystem-atmosphere relations: SMEAR, in: Physical and Physiological Forest Ecology, Springer, 471-487, 2013.

Haywood, J., and Shine, K.: The effect of anthropogenic sulfate and soot aerosol on the clear sky planetary radiation budget,
10   Geophysical Research Letters, 22, 603-606, 1995.

Haywood, J., and Boucher, O.: Estimates of the direct and indirect radiative forcing due to tropospheric aerosols: A review, Reviews of geophysics, 38, 513-543, 2000.

Hienola, A., Pietikäinen, J.-P., Jacob, D., Pozdun, R., Petäjä, T., Hyvärinen, A.-P., Sogacheva, L., Kerminen, V.-M., Kulmala, M., and Laaksonen, A.: Black carbon concentration and deposition estimations in Finland by the regional aerosol-climate
15   model REMO-HAM, Atmospheric Chemistry and Physics, 13, 4033, 2013.

Hyvärinen, A.-P., Kolmonen, P., Kerminen, V.-M., Virkkula, A., Leskinen, A., Komppula, M., Hatakka, J., Burkhart, J., Stohl, A., and Aalto, P.: Aerosol black carbon at five background measurement sites over Finland, a gateway to the Arctic, Atmospheric environment, 45, 4042-4050, 2011.

Karvosenoja, N., Kangas, L., Kupiainen, K., Kukkonen, J., Karppinen, A., Sofiev, M., Tainio, M., Paunu, V.-V., Ahtoniemi,
20   P., and Tuomisto, J. T.: Integrated modeling assessments of the population exposure in Finland to primary PM2. 5 from traffic and domestic wood combustion on the resolutions of 1 and 10 km, Air Quality, Atmosphere & Health, 4, 179-188, 2011.

Kulmala, M., Vehkamäki, H., Petäjä, T., Dal Maso, M., Lauri, A., Kerminen, V.-M., Birmili, W., and McMurry, P.: Formation and growth rates of ultrafine atmospheric particles: a review of observations, Journal of Aerosol Science, 35, 143-176, 2004.

Kulmala, M., Kontkanen, J., Junninen, H., Lehtipalo, K., Manninen, H. E., Nieminen, T., Petäjä, T., Sipilä, M., Schobesberger,
25   S., and Rantala, P.: Direct observations of atmospheric aerosol nucleation, Science, 339, 943-946, 2013.

Lack, D., and Cappa, C.: Impact of brown and clear carbon on light absorption enhancement, single scatter albedo and absorption wavelength dependence of black carbon, Atmospheric Chemistry and Physics, 10, 4207-4220, 2010.

Leskinen, A., Arola, A., Komppula, M., Portin, H., Tiitta, P., Miettinen, P., Romakkaniemi, S., Laaksonen, A., and Lehtinen, K.: Seasonal cycle and source analyses of aerosol optical properties in a semi-urban environment at Puijo station in Eastern
30   Finland, Atmospheric Chemistry and Physics, 12, 5647, 2012.

Lihavainen, H., Hyvärinen, A., Asmi, E., Hatakka, J., and Viisanen, Y.: Long-term variability of aerosol optical properties in northern Finland, Boreal Environment Research, 20, 526-541, 2015.

Lohmann, U., and Feichter, J.: Impact of sulfate aerosols on albedo and lifetime of clouds: A sensitivity study with the ECHAM4 GCM, Journal of Geophysical Research: Atmospheres, 102, 13685-13700, 1997.

Luoma, K., Virkkula, A., Aalto, P., Petäjä, T., and Kulmala, M.: Effects of algorithms on AOPs derived from AE-31 and PSAP at a boreal forest site, manuscript to be submitted to Atmospheric Measurement Techniques, 2018.

Mätzler, C.: MATLAB functions for Mie scattering and absorption, version 2, Institut für Angewandte Physik, University of Bern, 2002.

5 Pandolfi, M., Alados-Arboledas, L., Alastuey, A., Andrade, M., Angelov, C., Artiñano, B., Backman, J., Baltensperger, U., Bonasoni, P., and Bukowiecki, N.: A European aerosol phenomenology–6: scattering properties of atmospheric aerosol particles from 28 ACTRIS sites, Atmospheric Chemistry and Physics, 18, 7877-7911, 2018.

Saarikoski, S., Makela, T., Hillamo, R., Aalto, P. P., Kerminen, V., and Kulmala, M.: Physico-chemical characterization and mass closure of size-segregated atmospheric aerosols in Hyytiala, Finland, Boreal Environment Research, 10, 385-400, 2005.

10 Sandradewi, J., Prévôt, A. S., Szidat, S., Perron, N., Alfarra, M. R., Lanz, V. A., Weingartner, E., and Baltensperger, U.: Using aerosol light absorption measurements for the quantitative determination of wood burning and traffic emission contributions to particulate matter, Environmental Science & Technology, 42, 3316-3323, 2008.

Schnaiter, M., Linke, C., Möhler, O., Naumann, K. H., Saathoff, H., Wagner, R., Schurath, U., and Wehner, B.: Absorption amplification of black carbon internally mixed with secondary organic aerosol, Journal of Geophysical Research:
15 Atmospheres, 110, 2005.

Schuster, G. L., Dubovik, O., and Holben, B. N.: Angstrom exponent and bimodal aerosol size distributions, Journal of Geophysical Research: Atmospheres, 111, 2006.

Shen, Y., Virkkula, A., Ding, A., Wang, J., Chi, X., Nie, W., Qi, X., Huang, X., Liu, Q., and Zheng, L.: Aerosol optical properties at SORPES in Nanjing, east China, Atmospheric Chemistry and Physics, 18, 5265-5292, 2018.

20 Tunved, P., Hansson, H.-C., Kerminen, V.-M., Ström, J., Dal Maso, M., Lihavainen, H., Viisanen, Y., Aalto, P., Komppula, M., and Kulmala, M.: High natural aerosol loading over boreal forests, Science, 312, 261-263, 2006.

Twomey, S.: Aerosols, clouds and radiation, Atmospheric Environment, 25A, 2435-2442, 1991.

Weingartner, E., Saathoff, H., Schnaiter, M., Streit, N., Bitnar, B., and Baltensperger, U.: Absorption of light by soot particles: determination of the absorption coefficient by means of aethalometers, Journal of Aerosol Science, 34, 1445-1463, 2003.

25 Virkkula, A., Koponen, I., Teinilä, K., Hillamo, R., Kerminen, V. M., and Kulmala, M.: Effective real refractive index of dry aerosols in the Antarctic boundary layer, Geophysical Research Letters, 33, 2006.

Virkkula, A., Mäkelä, T., Hillamo, R., Yli-Tuomi, T., Hirsikko, A., Hämeri, K., and Koponen, I. K.: A simple procedure for correcting loading effects of aethalometer data, Journal of the Air & Waste Management Association, 57, 1214-1222, 2007.

Virkkula, A., Backman, J., Aalto, P., Hulkkonen, M., Riuttanen, L., Nieminen, T., Dal Maso, M., Sogacheva, L., De Leeuw,
30 G., and Kulmala, M.: Seasonal cycle, size dependencies, and source analyses of aerosol optical properties at the SMEAR II measurement station in Hyytiala, Finland, Atmospheric Chemistry and Physics, 11, 4445, 2011.

Zhang, R., Khalizov, A. F., Pagels, J., Zhang, D., Xue, H., and McMurry, P. H.: Variability in morphology, hygroscopicity, and optical properties of soot aerosols during atmospheric processing, Proceedings of the National Academy of Sciences, 105, 10291-10296, 2008.

Zieger, P., Aalto, P., Aaltonen, V., Äijälä, M., Backman, J., Hong, J., Komppula, M., Krejci, R., Laborde, M., and Lampilahti, J.: Low hygroscopic scattering enhancement of boreal aerosol and the implications for a columnar optical closure study, Atmospheric Chemistry and Physics, 15, 7247-7267, 2015.

Zotter, P., Herich, H., Gysel, M., El-Haddad, I., Zhang, Y., Močnik, G., Hüglin, C., Baltensperger, U., Szidat, S., and Prévôt, A. S.: Evaluation of the absorption Ångström exponents for traffic and wood burning in the Aethalometer-based source apportionment using radiocarbon measurements of ambient aerosol, Atmospheric Chemistry and Physics, 17, 4229-4249, 2017.

Ångström, A.: On the atmospheric transmission of sun radiation and on dust in the air, Geografiska Annaler, 11, 156-166, 1929.

Table 1: Average values of the AOPs for the PM10 particles. The average values were calculated from all valid data.

PM10	λ (nm)	mean ± SD	1 %	10 %	25 %	50 %	75 %	90 %	99 %
σ_{sca} (Mm⁻¹)	450	21.7 ± 23.2	1.7	4.5	7.5	14.1	26.7	48.4	113.7
	550	15.2 ± 16.7	1.3	3.4	5.5	9.8	18.2	33.3	82.4
	700	9.5 ± 10.4	0.8	2.3	3.6	6.3	11.3	20.2	52.2
σ_{bsca} (Mm⁻¹)	450	2.6 ± 2.4	0.2	0.6	1.1	1.9	3.3	5.5	11.6
	550	2.1 ± 1.9	0.2	0.5	0.9	1.5	2.6	4.4	9.3
	700	1.7 ± 1.6	-0.0	0.4	0.7	1.2	2.1	3.6	7.7
σ_{abs} (Mm⁻¹)	370	3.0 ± 4.2	0.1	0.5	1.0	1.9	3.7	6.7	18.3
	470	2.5 ± 2.9	0.1	0.4	0.8	1.6	3.0	5.4	14.5
	520	2.2 ± 2.5	0.1	0.4	0.7	1.4	2.6	4.7	12.4
	590	1.9 ± 2.2	0.1	0.3	0.6	1.2	2.4	4.2	10.9
	660	1.8 ± 2.0	0.1	0.3	0.6	1.1	2.2	3.8	10.0
	880	1.3 ± 1.5	0.1	0.2	0.5	0.9	1.6	2.9	7.3
	950	1.2 ± 1.3	0.0	0.2	0.4	0.8	1.5	2.6	6.5
ω_0	450	0.89 ± 0.07	0.66	0.81	0.87	0.91	0.94	0.96	0.99
	550	0.86 ± 0.08	0.59	0.76	0.83	0.87	0.92	0.95	0.98
	700	0.83 ± 0.09	0.52	0.72	0.79	0.84	0.89	0.93	0.98
b	450	0.13 ± 0.03	0.08	0.10	0.12	0.13	0.15	0.17	0.21
	550	0.15 ± 0.03	0.10	0.12	0.13	0.15	0.17	0.18	0.22
	700	0.19 ± 0.07	-0.01	0.13	0.16	0.19	0.22	0.25	0.40
α_{sca}	450/550	1.73 ± 0.52	0.23	1.02	1.49	1.82	2.09	2.29	2.58
	450/700	1.80 ± 0.55	0.31	1.00	1.53	1.88	2.17	2.38	2.80
	550/700	1.85 ± 0.65	0.23	0.95	1.53	1.95	2.25	2.50	3.16
α_{abs}	370/520	0.94 ± 0.57	-0.60	0.46	0.73	0.98	1.17	1.35	2.20
	370/950	0.94 ± 0.41	-0.33	0.50	0.78	0.99	1.14	1.27	1.85
	470/660	0.95 ± 0.62	-0.82	0.48	0.78	1.01	1.16	1.31	2.36
	470/950	1.00 ± 0.48	-0.52	0.54	0.85	1.06	1.19	1.31	2.05
	660/950	1.03 ± 0.68	-1.05	0.54	0.90	1.12	1.25	1.36	2.46
n	450	1.538 ± 0.067	1.322	1.475	1.510	1.541	1.571	1.604	1.694
	550	1.515 ± 0.067	1.287	1.449	1.488	1.520	1.548	1.579	1.666
	700	1.489 ± 0.090	1.244	1.375	1.451	1.499	1.535	1.570	1.726
k	450	0.020 ± 0.020	0.002	0.005	0.009	0.015	0.025	0.039	0.097
	550	0.020 ± 0.018	0.002	0.005	0.009	0.015	0.025	0.037	0.088
	700	0.022 ± 0.019	0.002	0.006	0.010	0.017	0.027	0.040	0.091
$\Delta F\delta^{-1}$ (Wm⁻²)	550	-22 ± 6	-33	-29	-27	-23	-19	-15	-1

Table 2: Average values of the AOPs for the PM1 particles. The average values were calculated from all valid data; thus compared with the PM10 average values, there is a 4-year shorter dataset.

PM1	λ (nm)	mean $\pm$ SD	1 %	10 %	25 %	50 %	75 %	90 %	99 %
σ_{sca} (Mm^{-1})	450	17.7 $\pm$ 19.2	1.2	3.1	5.6	11.3	22.3	40.4	96.1
	550	11.4 $\pm$ 13.0	0.8	2.1	3.6	7.1	14.1	26.1	64.8
	700	6.3 $\pm$ 7.5	0.4	1.2	2.0	3.8	7.6	14.4	37.4
σ_{bsca} (Mm^{-1})	450	2.2 $\pm$ 2.1	0.1	0.4	0.8	1.5	2.8	4.7	10.2
	550	1.7 $\pm$ 1.6	0.1	0.3	0.6	1.1	2.1	3.6	7.9
	700	1.2 $\pm$ 1.3	-0.2	0.2	0.4	0.9	1.6	2.8	6.2
σ_{abs} (Mm^{-1})	370	2.4 $\pm$ 3.0	0.0	0.3	0.7	1.5	2.9	5.3	15.3
	470	2.0 $\pm$ 2.3	0.0	0.3	0.6	1.3	2.4	4.3	11.9
	520	1.7 $\pm$ 2.0	0.0	0.3	0.5	1.1	2.1	3.7	10.2
	590	1.5 $\pm$ 2.8	0.0	0.2	0.5	1.0	1.9	3.4	8.9
	660	1.4 $\pm$ 1.6	0.0	0.2	0.5	0.9	1.8	3.1	8.1
	880	1.0 $\pm$ 1.2	0.0	0.2	0.3	0.7	1.3	2.3	5.9
	950	0.9 $\pm$ 1.0	0.0	0.1	0.3	0.6	1.2	2.0	5.2
ω_0	450	0.89 $\pm$ 0.07	0.65	0.80	0.86	0.90	0.94	0.96	0.99
	550	0.85 $\pm$ 0.09	0.56	0.73	0.80	0.86	0.91	0.95	0.99
	700	0.80 $\pm$ 0.10	0.46	0.65	0.73	0.80	0.86	0.91	0.98
b	450	0.14 $\pm$ 0.03	0.07	0.10	0.12	0.13	0.15	0.17	0.24
	550	0.16 $\pm$ 0.03	0.10	0.12	0.14	0.16	0.18	0.20	0.25
	700	0.21 $\pm$ 0.13	-0.18	0.11	0.16	0.21	0.25	0.32	0.62
α_{sca}	450/700	2.22 $\pm$ 0.44	0.88	1.70	1.99	2.28	2.51	2.66	2.95
	450/550	2.36 $\pm$ 0.55	0.74	1.76	2.09	2.41	2.66	2.87	3.70
	550/700	2.48 $\pm$ 0.81	0.25	1.73	2.16	2.52	2.82	3.13	4.69
α_{abs}	370/520	0.94 $\pm$ 0.82	-1.47	0.40	0.70	0.98	1.21	1.43	2.93
	370/950	0.96 $\pm$ 0.55	-0.82	0.45	0.77	1.03	1.20	1.38	2.36
	470/660	0.93 $\pm$ 0.85	-1.71	0.39	0.73	1.00	1.18	1.37	2.99
	470/950	1.04 $\pm$ 0.64	-1.02	0.51	0.86	1.11	1.27	1.46	2.81
	660/950	1.16 $\pm$ 0.95	-1.66	0.56	0.96	1.21	1.38	1.65	3.89
n	450	1.509 $\pm$ 0.056	1.350	1.441	1.479	1.513	1.542	1.570	1.634
	550	1.485 $\pm$ 0.054	1.340	1.422	1.457	1.488	1.517	1.542	1.599
	700	1.472 $\pm$ 0.071	1.298	1.395	1.436	1.473	1.507	1.538	1.669
k	450	0.023 $\pm$ 0.020	0.002	0.007	0.011	0.018	0.029	0.043	0.095
	550	0.023 $\pm$ 0.018	0.002	0.007	0.012	0.019	0.029	0.042	0.089
	700	0.027 $\pm$ 0.019	0.003	0.009	0.015	0.023	0.033	0.047	0.094

Table 3: Slopes of the trends (in absolute values and in estimated percentages per year) and their statistical significance. The lower and upper limits in the 95 % confidence interval for different optical properties are also shown. The trend in the percentage was determined by comparing the slope of the trend with the overall median of the data.

		PM10					**PM1**				
	λ	**Trend**		**Lower**	**Upper**	**p-value**	**Trend**		**Lower**	**Upper**	**p-value**
	(nm)	**(yr^{-1})**		**(yr^{-1})**	**(yr^{-1})**		**(yr^{-1})**		**(yr^{-1})**	**(yr^{-1})**	
σ_{sca} **(Mm^{-1})**	550	-0.34	-3 %	-0.52	-0.19	< 0.01	-0.30	-4 %	-0.55	-0.14	< 0.05
σ_{bsca} **(Mm^{-1})**	550	-0.043	-3 %	-0.075	-0.022	< 0.01	-0.054	-5 %	-0.089	-0.015	< 0.01
σ_{abs} **(Mm^{-1})**	520	-0.095	-7 %	-0.146	-0.061	< 0.01	-0.144	-13 %	-0.176	-0.098	< 0.01
ω_0	550	3.4e-3	0.4 %	2.0e-3	4.8e-3	< 0.01	7.9e-3	1 %	3.4e-3	11e-3	< 0.01
b	550	1.3e-3	1 %	1.0e-3	1.8e-3	< 0.01	1.6e-3	1 %	0.8e-3	2.7e-3	< 0.01
α_{sca}	450/700	0.012	0.6 %	-0.00	0.023	0.06	0.014	0.6 %	0.003	0.026	< 0.01
α_{abs}	370/950	-1.8e-3	-0.2 %	-5.4e-3	1.4e-3	0.53	-2.9e-3	-0.3 %	-9.6e-3	8.3e-3	0.56
n	550	-2.0e-3	-0 %	-4.0e-3	6.0e-4	0.13	-5.6e-3	-0.4 %	-8.1e-3	-3.3e-3	< 0.01
k	550	-7.5e-4	-5 %	-10e-4	-4.9e-4	< 0.01	-1.4e-3	-7 %	-2.0e-3	-1.0e-3	< 0.01
$\Delta F \delta^{-1}$ **(Wm^{-2})**	550	-0.39	-2 %	-0.54	-0.29	< 0.01					
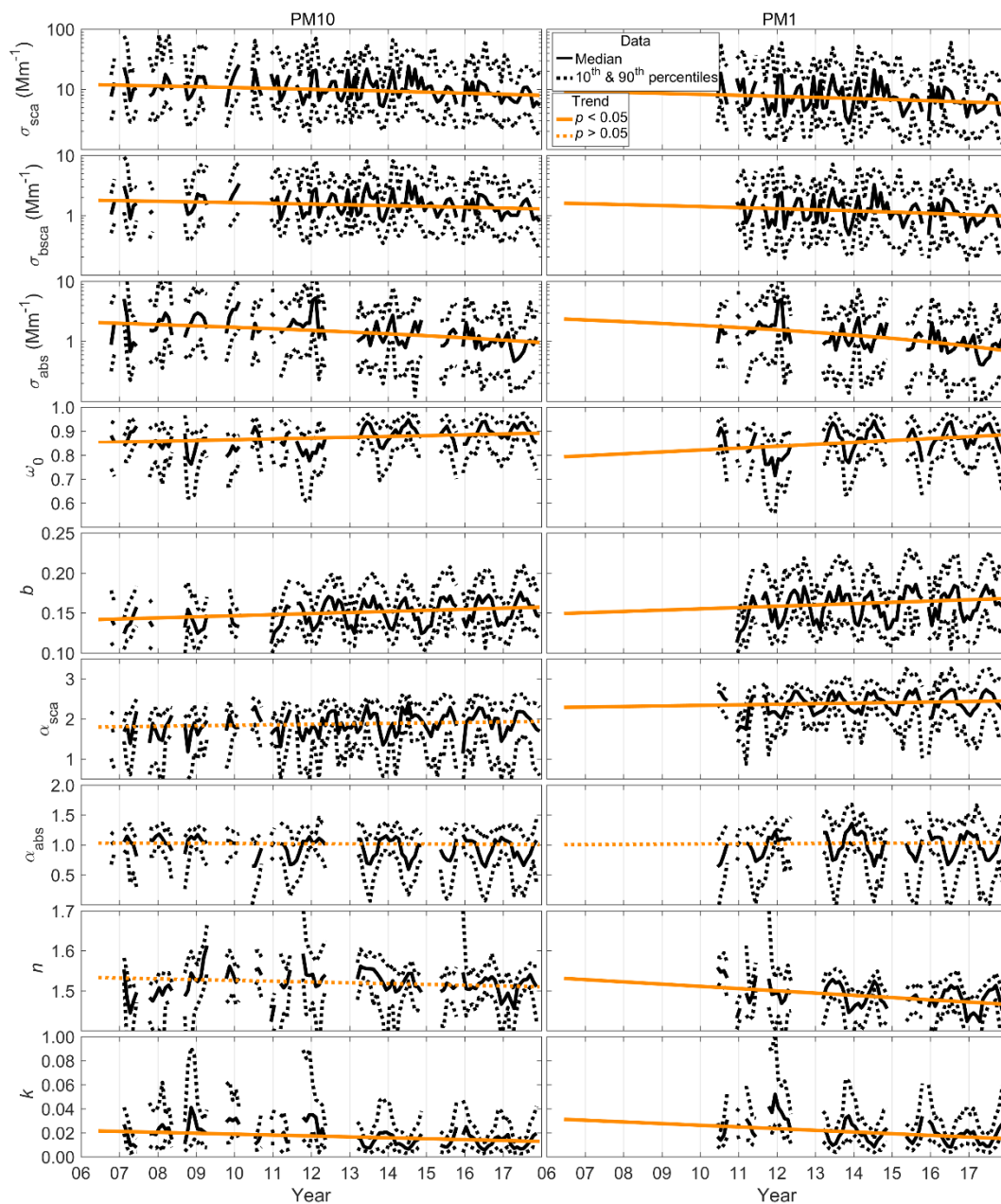
Figure 1: Time series of the AOPs. The uniform black line presents the monthly median and the dotted black lines present the monthly 10th and 90th percentiles. The trends (see Table 3) of the AOPs are shown with orange lines. If the trend was statistically significant, the line is uniform and if the p-value of the trend was > 0.05, the line is dashed.
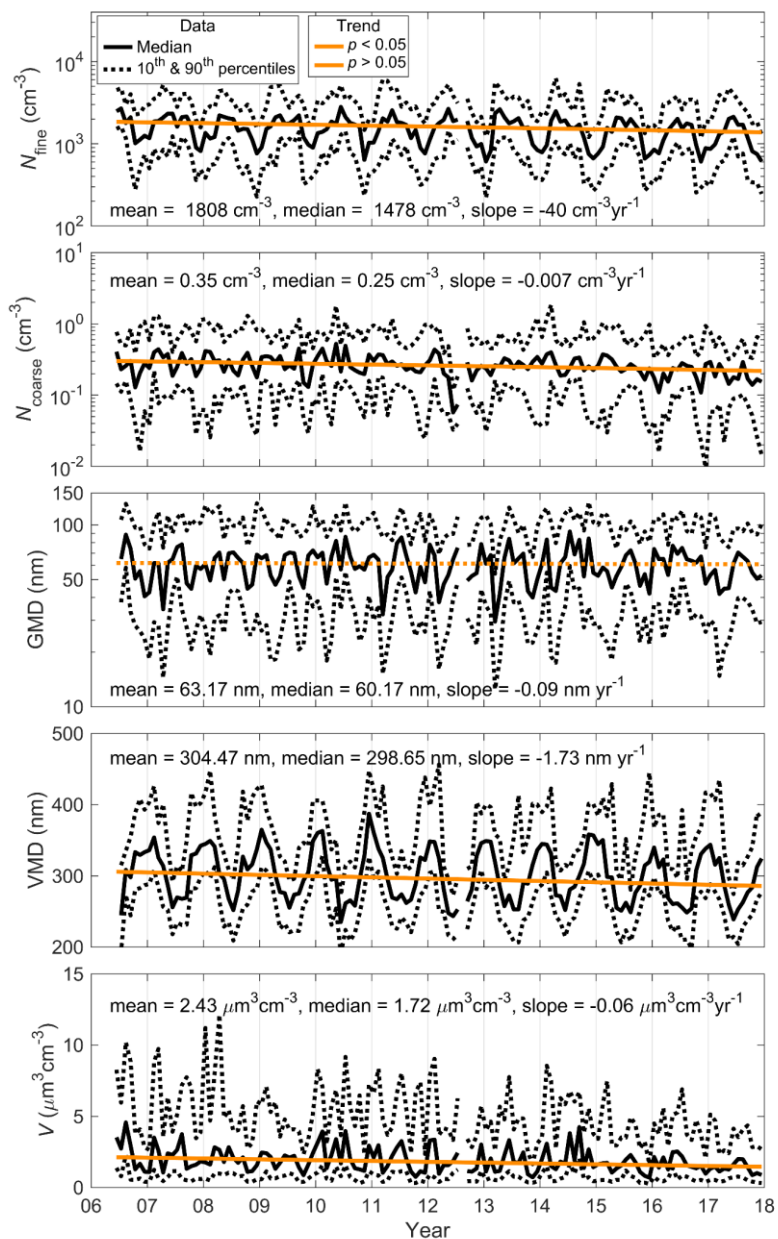
Figure 2: Time series and trends of the fine and coarse particle number concentration, GMD, VMD and total particle volume (V). The GMD, VMD and V were calculated for the PM1 particles only. The slopes of the trends and the mean and median values of the variables are also marked in the subfigures.
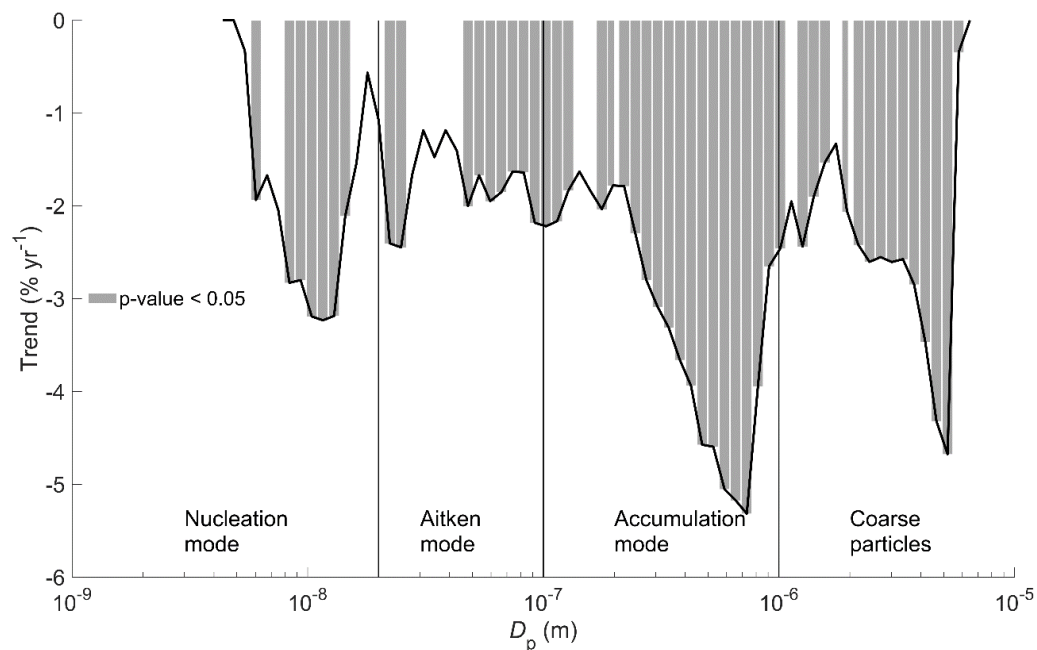
Figure 3: Trend analysis for the size distribution. The average trend in the percentages is shown with a solid line. The gray bars
5 **mark the size ranges, in which the trend was statistically significant (*p*-value < 0.05). The typical borders of the nucleation, Aitken,**
accumulation and coarse particle modes are marked with vertical lines.
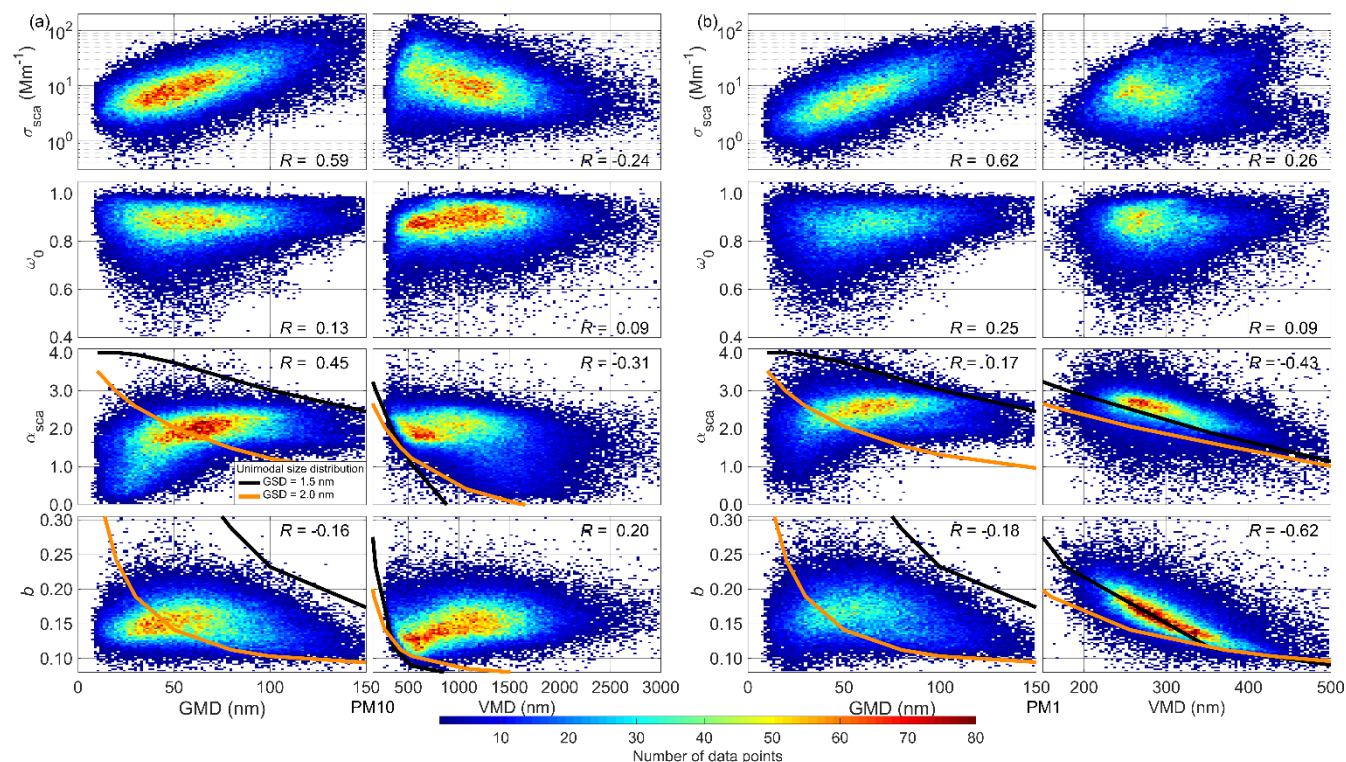
Figure 4: Relationships between the various AOPs, GMD and VMD for a) PM10 and b) PM1 particles. The relationship between the AOPs and the GMD are shown in the left column and the relationship between the AOPs and the VMD in the right column. The correlation coefficients of the linear regressions are given in each subfigure. The color-coding represents the number of data points in a grid point. In each subfigure, there are 100 grid points on both axes, making 1000 grid points in total. The orange and black lines represent the values calculated from the unimodal size distributions, which were generated for different GMDs with geometric standard deviation GSD = 2.0 and 1.5 nm. The scattering was modeled from the generated size distribution at wavelengths 450, 550, and 700 nm with a refractive index $m = 1.517 + 0.19i$.
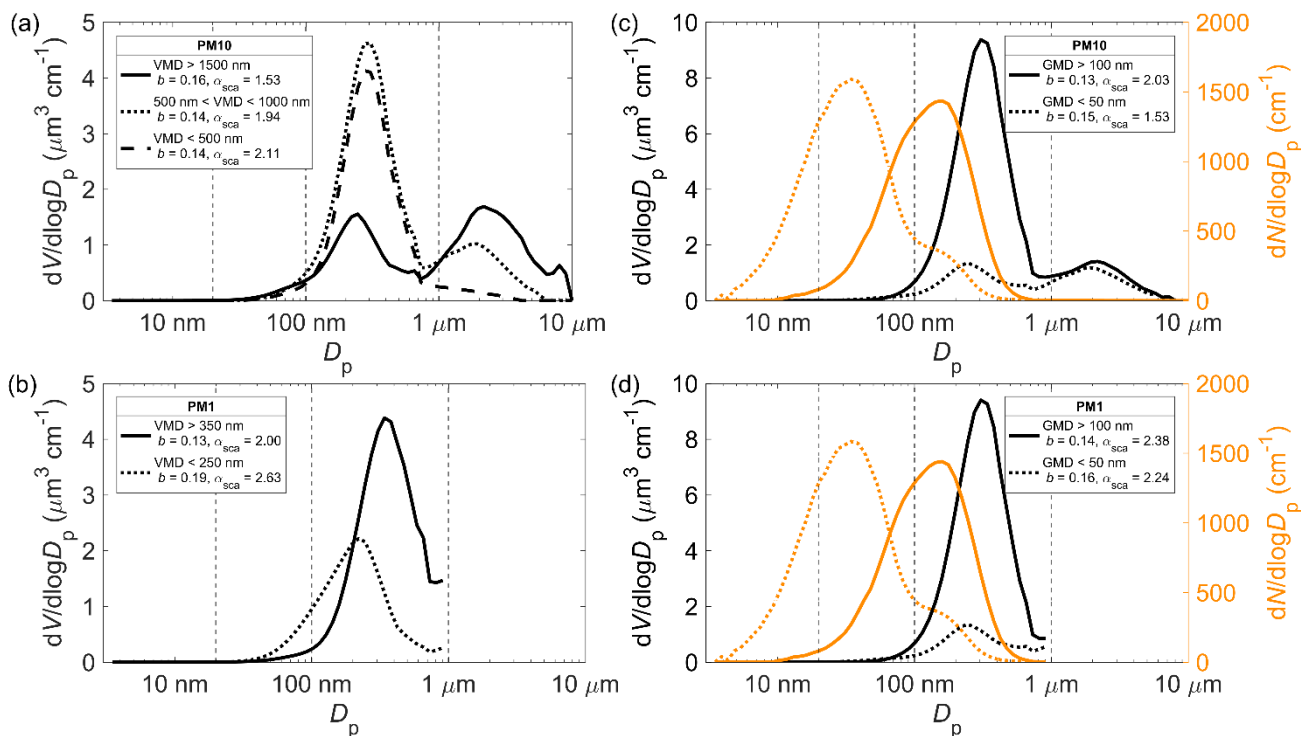
Figure 5: Median volume and number size distributions for the various VMD and GMD limits. The median b and α_{sca} for the VMD and GMD limits are given in each legend box. The vertical grid lines represent the typical diameter limits for the nucleation, Aitken, accumulation and coarse particle modes (same as in Fig. 3). a) Volume size distribution for different PM10 VMD limits. b) Volume size distribution for different PM1 VMD limits. c) Volume and number size distribution for different PM10 GMD limits. d) Volume and number size distribution for different PM1 GMD limits.
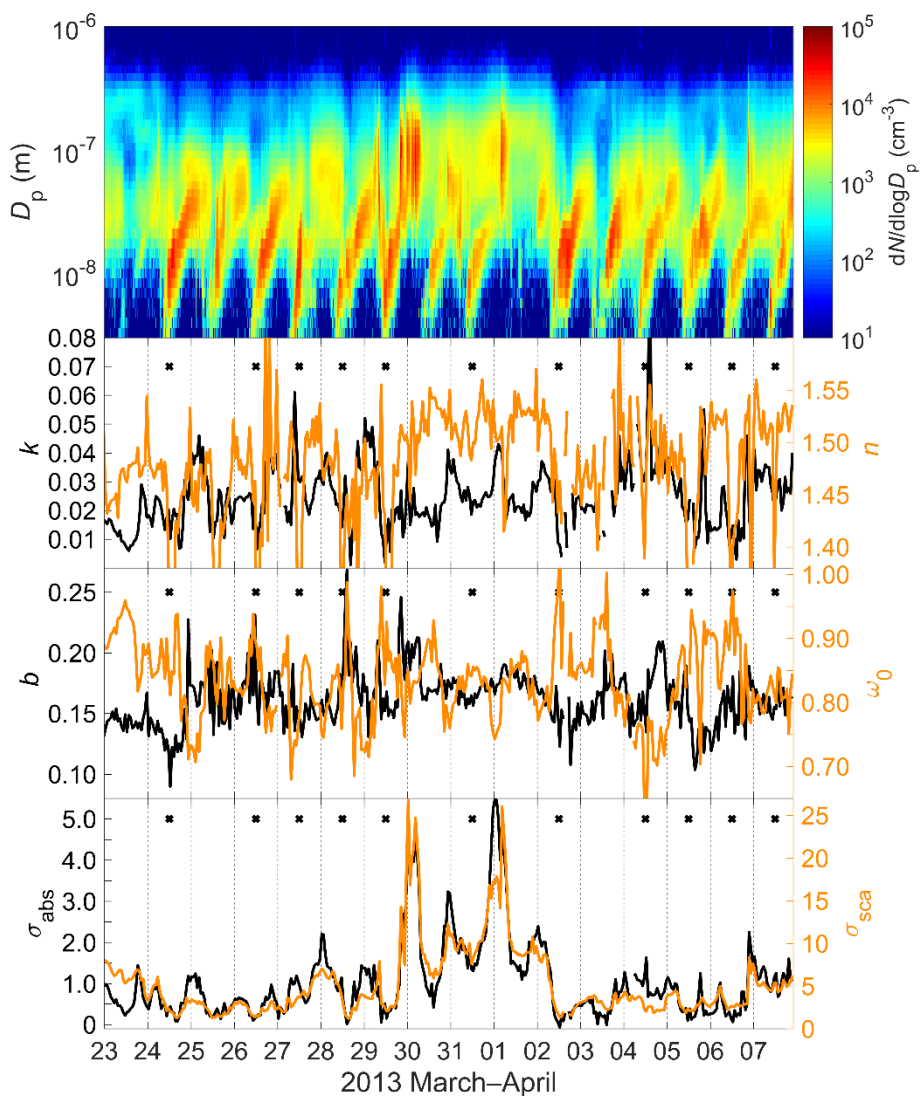
Figure 6: An example of size distribution and AOPs of the PM1 particles from the spring of 2013, when several new particle formation events occurred. The classified event days are marked with black crosses.
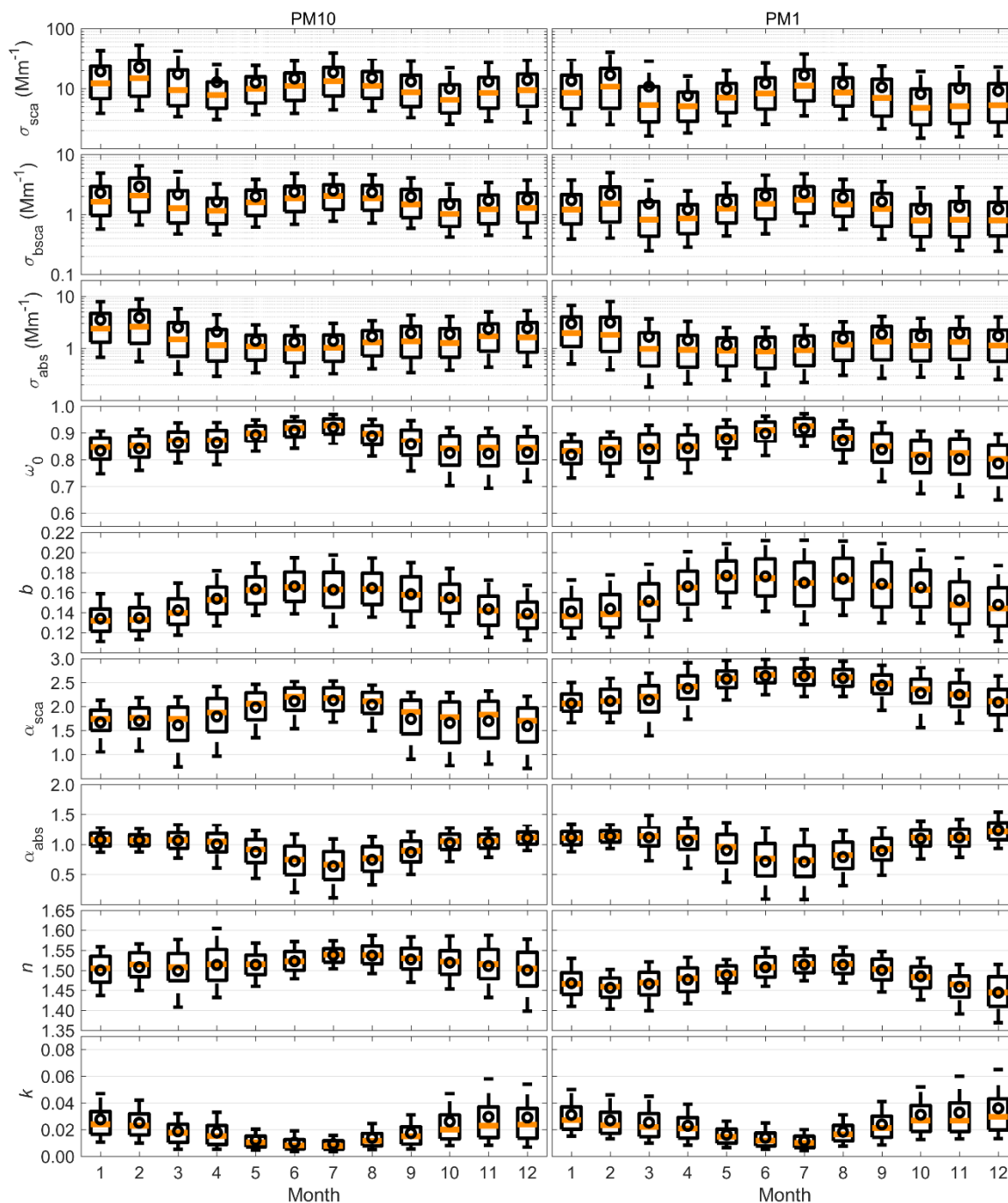
Figure 7: Seasonal variation in the aerosol optical properties. The boxes represent the 25th and 75th percentiles and the whiskers the 10th and 90th percentiles of the data. The orange line is the median and the mean is represented with a black circle. The left column shows the seasonal variation of the PM10 particles and the right column shows the seasonal variation of the PM1 particles.
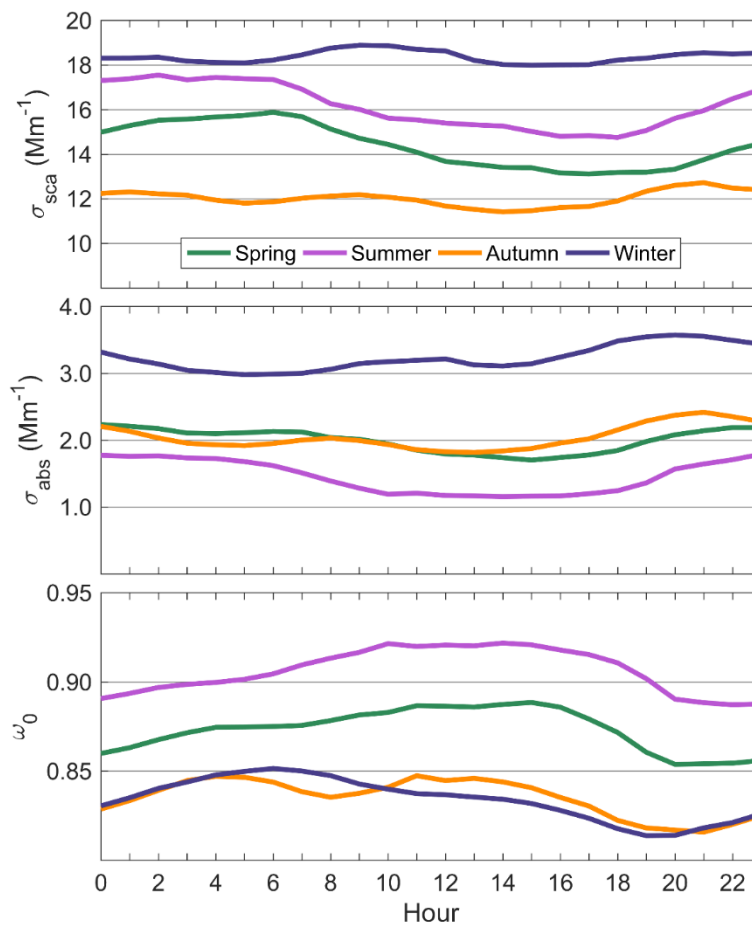
Figure 8: Diurnal variation in σ_{sca}, σ_{abs} and ω_0 for four seasons (Spring: March–May, Summer: June–August, Autumn: September–November, Winter: December–February), presented by different colored lines. The diurnal variation is shown as the mean values for the PM10 particles.
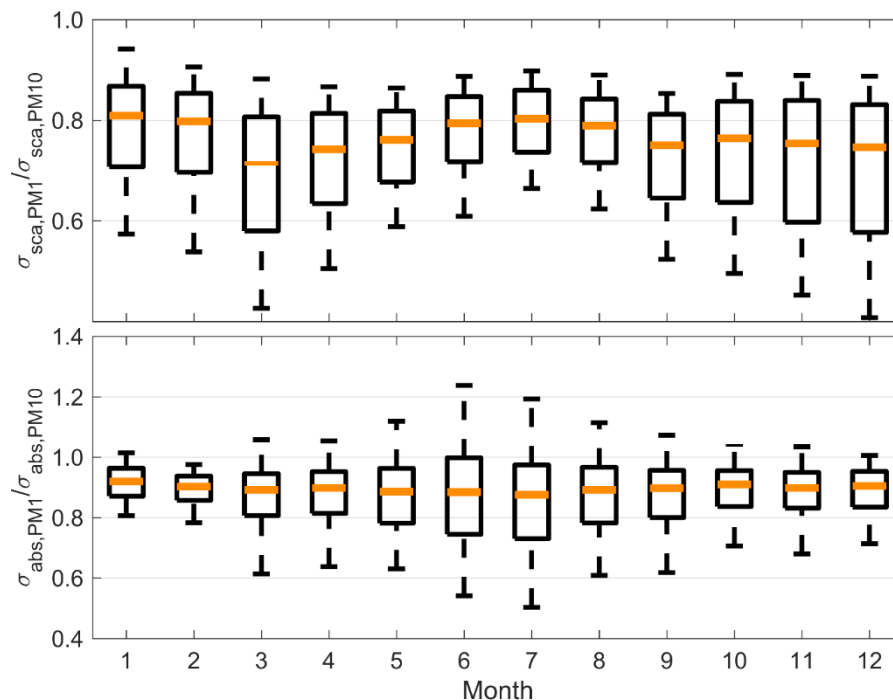
Figure 9: Seasonal variation in the PM1/PM10 ratio for both σ$_{sca}$ and σ$_{abs}$. The explanations for the boxplots are the same as in Fig. 7.
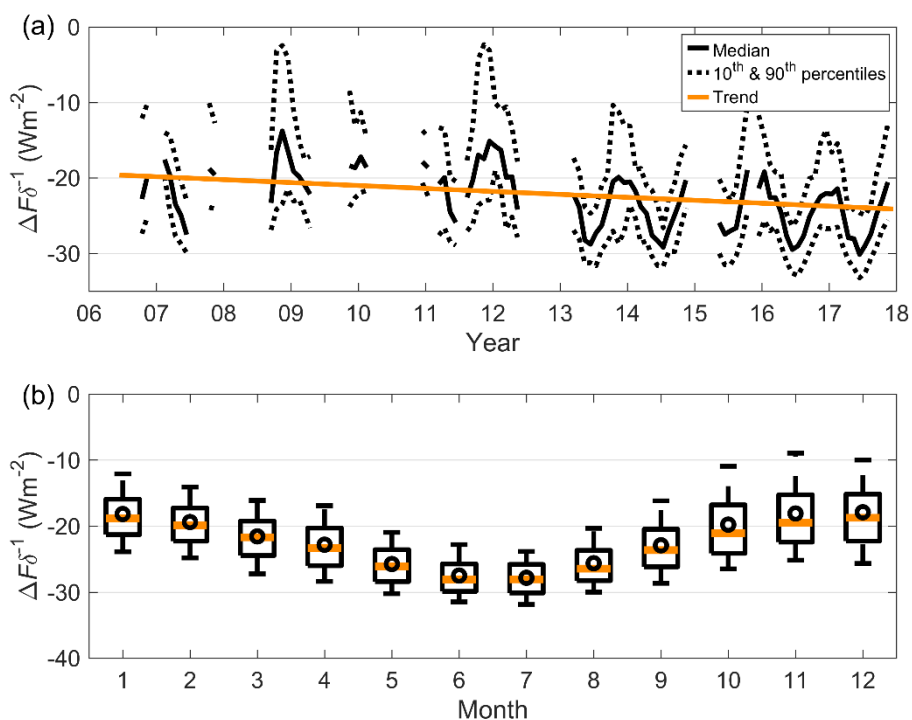
Figure 10: Variations in the radiative forcing efficiency RFE = $\Delta F\delta^{-1}$ at SMEAR II in 2006 – 2018. a) Time series and the trend of the RFE. b) Seasonal variation in the RFE. The explanations for the boxplots are the same as in Fig. 7.
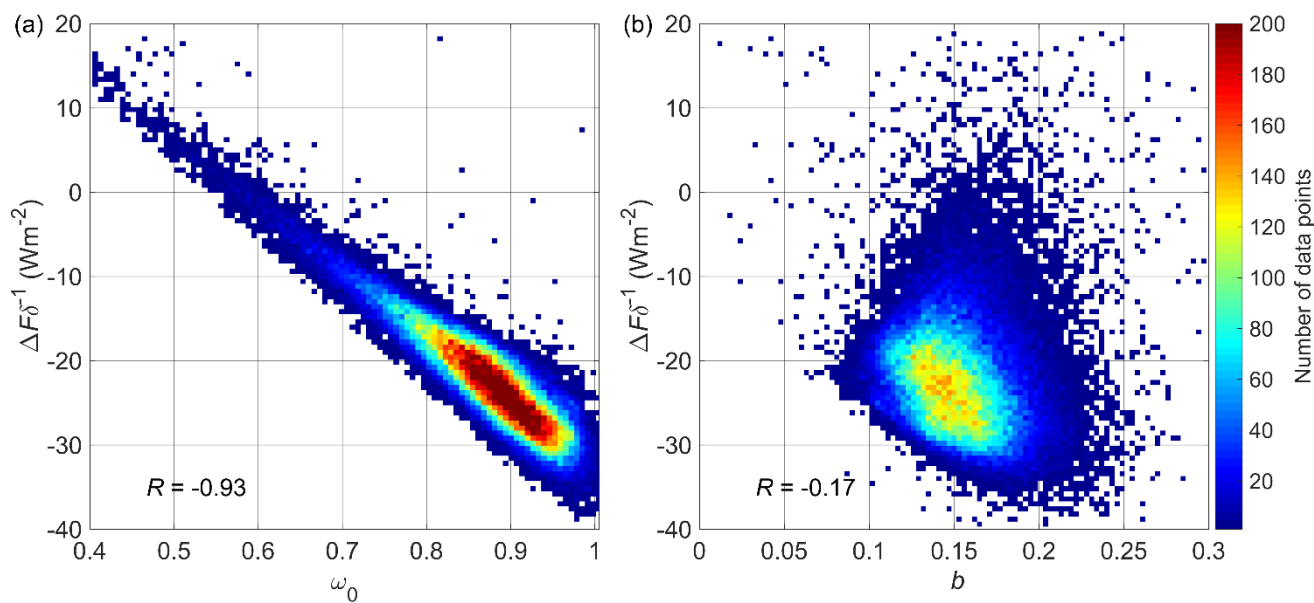
Figure 11: RFE ($\Delta F\delta^{-1}$) as a function of a) single-scattering albedo (ω_0) and b) backscatter fraction (b) at λ = 550 nm. The coloring indicates the concentration of the data points in a single grid point. In each figures, there are 100 grid points on both axes, making 1000 grid points in total.
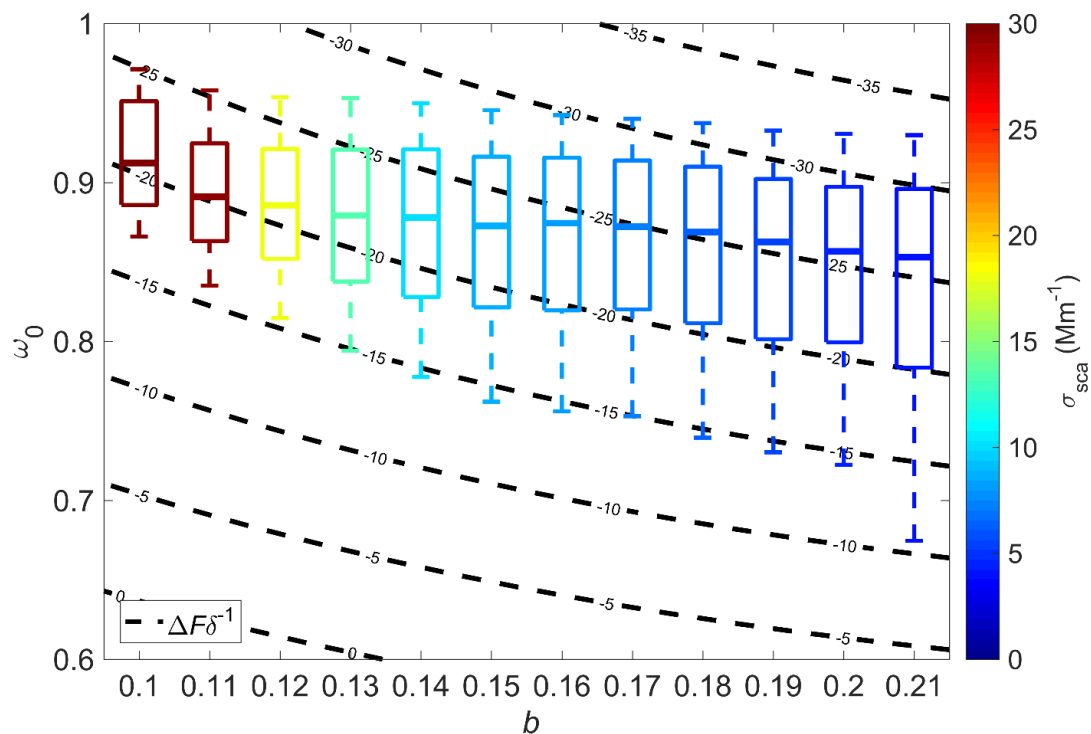
Figure 12: Relationships between ω_0, b and RFE. The RFE is shown as the dashed isolines in the background. The boxes represent the data measured at SMEAR II and they are colored by the median σ_{sca}. The explanation for the boxplots is the same as in Fig. 7.